PB82-110057

A Two-Stage Particle Fractionator Using Large Pore Nuclepore Surfaces

Duke Univ.
Durham, NC

Prepared for

Environmental Sciences Research Lab.
Research Triangle Park, NC

Jun 81

U.S. Department of Commerce
National Technical Information Service
NTIS.

BEGIN FIRST LINE OF TEXT HERE
CENTER OF PAGE
TOP OF IMAGE AREA

EPA-600/2-81-107
June 1981

PB82-110057

DROPPED HEAD; BEGIN SECTIONS HERE

A TWO STAGE PARTICLE FRACTIONATOR USING LARGE PORE NUCLEPORE SURFACES

by

Gale H. Buzzard
Richard D. Parker
Duke University
Durham, North Carolina 27706

and

John P. Bell
Atmospheric Chemistry and Physics Division
Environmental Sciences Research Laboratory
Research Triangle Park, N. C. 27711

Grant No. R-803018

Project Officer

John P. Bell
Atmospheric Chemistry & Physics Division
Environmental Sciences Research Laboratory
Research Triangle Park, NC 27711

REPRODUCED BY
NATIONAL TECHNICAL
INFORMATION SERVICE
U.S. DEPARTMENT OF COMMERCE
SPRINGFIELD, VA 22161

ENVIRONMENTAL SCIENCES RESEARCH LABORATORY
OFFICE OF RESEARCH AND DEVELOPMENT
U.S. ENVIRONMENTAL PROTECTION AGENCY
RESEARCH TRIANGLE PARK, NORTH CAROLINA 27711

6-1/2"
9-1/8"
BEGIN LAST LINE OF TEXT
3/8"
BOTTOM OF IMAGE AREA; OUTSIDE DIMENSION FOR TABLES AND ILLUSTRATIONS
PAGE NUMBER
EPA Form 2350-4 (4-70)
(PREVIOUSLY CIN. EPA FORM 2971)
TYPING GUIDE SHEET

TECHNICAL REPORT DATA
(Please read Instructions on the reverse before completing)

1. REPORT NO. EPA-600/2-81-107	2.
3. RECIPIENT'S ACCESSION NO. PB82 110057	
4. TITLE AND SUBTITLE A TWO STAGE PARTICLE FRACTIONATOR USING LARGE PORE NUCLEPORE SURFACES	5. REPORT DATE June 1981
	6. PERFORMING ORGANIZATION CODE
7. AUTHOR(S) Gale H. Buzzard, Richard D. Parker and John P. Bell	8. PERFORMING ORGANIZATION REPORT NO.
9. PERFORMING ORGANIZATION NAME AND ADDRESS Department of Mechanical Engineering & Material Sciences Duke University Durham, N. C. 27706	10. PROGRAM ELEMENT NO. CAFA1D/01-0429 (FY-81)
	11. CONTRACT/GRANT NO. R 803018
12. SPONSORING AGENCY NAME AND ADDRESS Environmental Sciences Research Laboratory - RTP, NC Office of Research and Development U.S. Environmental Protection Agency Research Triangle Park, N. C. 27711	13. TYPE OF REPORT AND PERIOD COVERED
	14. SPONSORING AGENCY CODE EPA/600/09

15. SUPPLEMENTARY NOTES

16. ABSTRACT

A fundamental study of the collection efficiency resulting from inertial deposition of particles onto large pore Nuclepore filters has been conducted. The theoretical procedure involved the solution of the Navier-Stokes equations for steady flow through a representative filter pore. Stokes' drag forces were applied to a particle in the flow field and used to determine its trajectory. The critical trajectory for deposition was found, and the collection efficiency was determined. The solutions were obtained numerically. The study was restricted to continuum flow and assumed negligible particle diffusion.

The theory was used to investigate the influence of pore Reynolds number, particle density, filter thickness, and filter porosity upon the collection efficiency.

Experimental collection efficiencies were obtained for laboratory generated particles. The filters were analyzed using optical fluorescence techniques. The experimental results obtained for a liquid aerosol are in good agreement with the theory and are viewed as validation of the impaction theory developed. The experimental results obtained for a solid aerosol fall well below the theoretical predictions and are viewed as an indication of particle bounce for a non-sticky aerosol.

17. KEY WORDS AND DOCUMENT ANALYSIS

a. DESCRIPTORS	b. IDENTIFIERS/OPEN ENDED TERMS	c. COSATI Field/Group

18. DISTRIBUTION STATEMENT RELEASE TO PUBLIC	19. SECURITY CLASS *(This Report)* UNCLASSIFIED	21.
	20. SECURITY CLASS *(This page)* UNCLASSIFIED	22. PRICE

EPA Form 2220-1 (Rev. 4-77) PREVIOUS EDITION IS OBSOLETE

DISCLAIMER

This report has been reviewed by the Environmental Sciences Research Laboratory, U.S. Environmental Protection Agency, and approved for publication. Approval does not signify that the contents necessarily reflect the views and policies of the U.S. Environmental Protection Agency, nor does mention of trade names or commercial products constitute endorsement or recommendation for use.

BEGIN FIRST LINE OF TEXT HERE
TYPING GUIDE SHEET
CENTER OF PAGE
TOP OF IMAGE AREA
DROPPED HEAD BEGIN SECTIONS HERE

ABSTRACT

A fundamental study of the collection efficiency resulting from inertial deposition of particles onto large pore Nuclepore filters has been conducted. The principle objectives of the study have been to develop a computational procedure for predicting the filter collection efficiency, to verify the predictions experimentally, and to apply the procedure to investigate the effects of pore Reynolds number, particle density, filter thickness, and filter porosity upon the efficiency. The study has been restricted to the consideration of continuum flow and negligible diffusion forces.

The theoretical procedure involved the solution of the Navier-Stokes equations for steady flow through a representative filter pore. Stokes' drag forces were then applied to a particle in the flow field, to determine its equations of motion and trajectory. The critical trajectory for deposition to occur was found, and from this, the collection efficiency was determined. The solutions for the flow field, the trajectories, and the collection efficiency were achieved numerically on a digital computer.

The flow field through a plexiglas model of the filter has been studied experimentally using a glycerin-water mixture, and a flow visualization technique which used dye to trace experimental streamlines. The streamlines were photographed and compared to the streamlines obtained from the theoretical flow field solutions.

The theory was used to investigate the influence of the pore Reynolds number, the particle density, the filter thickness, and the filter porosity upon the collection efficiency versus particle diameter.

Experimental collection efficiencies were obtained by generating monodisperse, uniform diameter particles, and collecting them on a test filter followed in series by a backup filter. The filters were analyzed, using an optical fluorescence technique, to determine the amount of particulate matter deposited on each filter. Assuming all particles which passed through the test filter were caught by the backup filter, the experimental collection efficiency was determined. The experimental results obtained for a liquid aerosol were in good agreement with the theory developed. The experimental results obtained for a solid aerosol fell well below the theoretical predictions and are viewed as an indication of particle bounce for other than a sticky aerosol.

This report was submitted in fulfillment of Grant No. R-80318 by Duke University under the sponsorship of the U.S. Environmental Protection Agency. This report covers a period from March 15, 1974 to March 14, 1980, and work was completed as of March 14, 1980.

BEGIN LAST LINE OF TEXT
BOTTOM OF IMAGE AREA OUTSIDE DIMENSIONAL FOR TABLES AND ILLUSTRATIONS
3/8"
PAGE NUMBER
EPA-287 (Rev.) (4-76)

CONTENTS

Abstract iii
Figures vi
Tables viii
Symbols ix
Acknowledgement xiv

1. Introduction 1
   - Background 1
   - Review of Previous Work 2
   - Present Work 3
2. Conclusions 6
3. Flow Field Through A Circular Pore 9
   - Introduction 9
   - Theory 9
   - Numerical Solution 16
   - Results of the Flow Field Solution 22
   - Flow Visualization Model 28
4. Particle Trajectories and Filter Impaction Efficiencies. 38
   - Introduction 38
   - Calculation of the Velocity Fields 38
   - Theory for Particle Trajectories 39
   - Numerical Solution 42
   - Impaction Efficiencies 43
   - Results and Discussion 47
5. Impaction Efficiency Study. 51
   - Introduction 51
   - The Effect of Pore Reynolds Number 51
   - The Effect of Particle Density 51
   - The Effect of Filter Thickness 51
   - The Effect of Filter Porosity. 56
6. Experimental Collection Efficiencies. 60
   - Introduction 60
   - Experimental Procedures. 60
   - Results. 62

References 66

Appendices

A. Finite Difference Equations 68

Preceding page blank

BEGIN FIRST LINE OF TEXT HERE
TYPING GUIDE SHEET
CENTER OF PAGE
TOP OF IMAGE AREA
DROPPED HEAD: BEGIN SECTIONS HERE

FIGURES

Number		Page
1	Present work compared with earlier theories	7
2	Theoretical model of a circular pore.	10
3	Boundary conditions on U and V in the R-Z coordinate system	13
4	Boundary conditions on ψ and ω in the R-Z coordinate system	15
5	Boundary conditions on ψ and ω in the combined R-Z and R-η coordinate system	17
6	Finite difference grid network.	20
7	Convergence of ψ at a point near the pore entrance corner as the grid spacing approaches zero.	23
8	Convergence of U and V at a point near the pore entrance corner as the grid spacing approaches zero	24
9	Streamlines through a circular pore. Re = 1.	25
10	Streamlines through a circular pore. Re = 2.	26
11	Streamlines through a circular pore. Re = 3.	27
12	Apparatus for the flow visulaization experiment	29
13	Plexiglas test plate for the flow visualization experiment.	30
14	Test plate with boundaries imposed upon the theoretical and physical pore models.	31
15	Experimental temperature-viscosity curve for the glycerin-water mixture.	33
16	Experimental streamlines compared to the theoretical streamlines. Re = 5.	35

BEGIN LAST LINE OF TEXT
BOTTOM OF IMAGE AREA OUTSIDE DIMENSION FOR TABLES AND ILLUSTRATIONS
3/8"
PAGE NUMBER
EPA-237 (Chm.) (4-70)

Figures (cont'd)

Number		Page
17	Experimental streamlines compared to the theoretical streamlines. Re = 8	36
18	Theoretical particle trajectories for different diameter particles	44
19	Theoretical particle trajectories for different upstream radial starting positions	45
20	The criterion used to determine particle impaction	46
21	Convergence of the impaction efficiency as the finite difference grid spacing decreases	48
22	Estimate of the effect of further grid refinement on the impaction efficiency curve.	49
23	Effect of Reynolds number on the impaction efficiency.	52
24	Effect of particle density on the impaction efficiency. Re = 1.	53
25	Effect of particle density on the impaction efficiency. Re = 2.	54
26	Effect of particle density on the impaction efficiency. Re = 3.	55
27	Illustration of the ratio R_{crit}/β as porosity approaches 100%.	59
28	Experimental collection efficiencies compared with the model. Face velocity = 10 cm/s.	63
29	Experimental collection efficiencies compared with the model. Face velocity = 20 cm/s.	64

TABLES

Number		Page
1	Actual Reynolds numbers for the flow visualization experiment. Average Reynolds number = 5	34
2	Actual Reynolds numbers for the flow visualisation experiment. Average Reynolds number = 8	34
3	The effect of filter thickness on the impaction efficiency	56
4	The effect of filter porosity on the impaction efficiency	57
5	The impaction efficiency and the ratio R_{crit}/β as the porosity approaches 100%	58

LIST OF SYMBOLS

A_f -- total filter area

C -- Cunningham slip correction factor

D_p -- droplet diameter

d_p -- particle diameter

D_{pore} -- pore diameter

dn -- size of the last radial grid adjacent to the stream tube boundary

E -- impaction efficiency

F_z -- the gravity term in the Navier-Stokes equations

f -- frequency of vibration of the orifice in the particle generator

f -- general dilution factor

f_t, f_b -- dilution factors for the test and backup filters

h -- general grid spacing

h_o -- general grid spacing representing the finest finite difference grid network used

h_d -- downstream axial grid spacing

h_r -- radial grid spacing

h_u -- upstream axial grid spacing

h_Z -- axial grid spacing inside the pore

h_{Z_d} -- the downstream grid adjacent to the pore exit, expressed in the Z coordinate system

h_{Z_u} -- the upstream grid adjacent to the pore entrance, expressed in the Z coordinate system

Symbols (cont'd)

k	-- general transformation constant
k_1, k_2, k_3	-- derivative approximations associated with the Runge-Kutta integration
k_d, k_u	-- downstream and upstream transformation constants
Kn	-- Knudsen number
n	-- general normal direction
P	-- filter porosity
p	-- effective pressure
p^1	-- actual pressure
Q	-- flow rate
R	-- dimensionless radial coordinate
r	-- actual radial coordinate
R_1	-- pore radius
R_2	-- stream tube radius
R_{crit}	-- starting radial position of a particle corresponding to its critical trajectory
r_p	-- particle radius
R_{part}	-- particle radius
R_{pore}	-- pore radius
Re	-- pore Reynolds number
T	-- filter thickness
t	-- time
U	-- dimensionless axial component of the particle velocity
U_1	-- average velocity through the pore
U_∞	-- upstream and downstream fluid velocity
U_p	-- dimensionless axial component of the particle velocity

Symbols (cont'd)

V -- dimensionless radial component of the fluid velocity

V_b -- photomultiplier output for backup filter

$\bar{V}_f$ -- fluid velocity

$\bar{V}_p$ -- particle velocity

V_p -- dimensionless radial component of the particle velocity

v_r -- actual radial velocity

V_t -- photomultiplier output for the test filter

v_z -- actual axial velocity

X_1 -- first derivative of η with respect to Z

X_2 -- first derivative of X_1 with respect to Z

Z -- dimensionless axial coordinate

z -- actual axial coordinate

Z_o -- half the dimensionless pore length

z_o -- half the actual pore length

β -- dimensionless stream tube radius

Δ -- step size control criterion for Runge-Kutta integration

ε -- general error estimate

η -- general transformed axial coordinate

η_d, η_u -- downstream and upstream transformed axial coordinates

λ -- mean free path for air molecules

μ_f -- fluid dynamic viscosity

ν -- kinematic viscosity

ξ -- inertial parameter or Stokes number

ρ_f -- fluid density

ρ_p -- particle density

Preceding page blank

Symbols (cont'd)

ϕ -- azimuthal coordinate

ψ -- stream function

ω -- vorticity

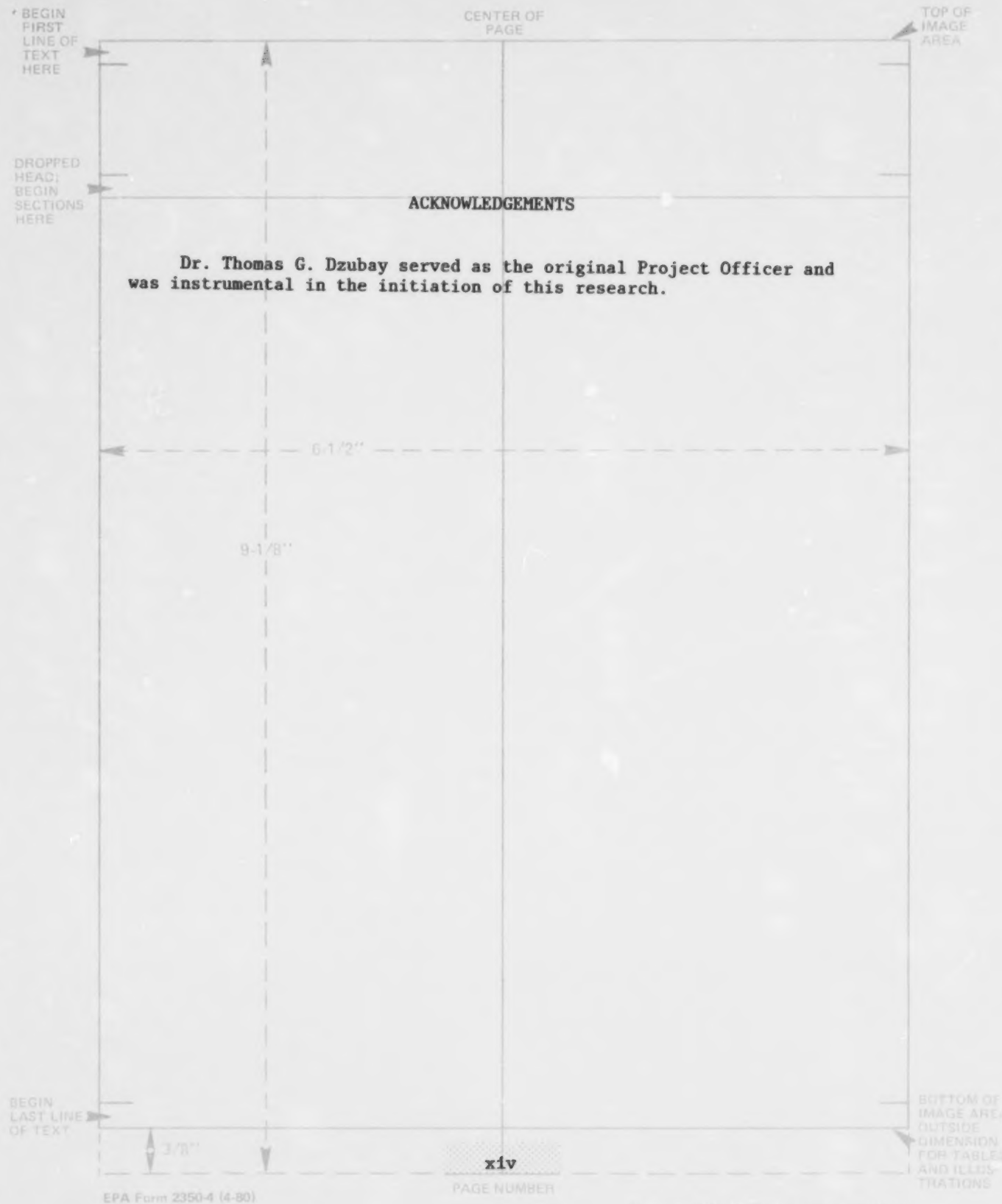

ACKNOWLEDGEMENTS

Dr. Thomas G. Dzubay served as the original Project Officer and was instrumental in the initiation of this research.

EPA Form 2350-4 (4-80)
(PREVIOUSLY CIN. EPA FORM 287)

TYPING GUIDE SHEET

BEGIN FIRST LINE OF TEXT HERE
TYPING GUIDE SHEET
CENTER OF PAGE
TOP OF IMAGE AREA
DROPPED HEAD: BEGIN SECTIONS HERE

SECTION 1

INTRODUCTION

BACKGROUND

Size selective techniques are essential to current air quality sampling technology. Whitby et al. (1) have shown that the volume of particulate matter in the atmosphere occurs in two distinct size ranges, with a relative minimum occurring at a particle diameter of about 2μm. Hatch and Gross (2) have discussed the size selective filtration characteristics of the human respiratory system. The upper respiratory tract may be approximated by an efficiency curve[1] ranging from 100% removal of 10μm diameter particles, to 0% removal of particles smaller than 2μm. The 50% cut-point (particle diameter for which the collection efficiency[2] is 50%) occurs at a diameter of 3.5μm. For these reasons it would be desirable to have a two stage sampler whose first stage would have a 50% cut-point adjustable between 2μm and 3.5μm. This has commonly been achieved by using a cyclone separator as the first stage. Large pore Nuclepore[3] filters may represent an improvement over the cyclone separators. Whereas cyclones do not permit the analysis of the particulate they remove from the airstream, Nuclepore filters may be analyzed very easily using X-ray fluorescence techniques. Also, it is possible to predict theoretical efficiencies for Nuclepore filters, and thus determine performance curves which would enable the cut-point to be adjusted as desired. The purpose of the present study has been to develop and validate the theory necessary to predict the performance curves.

Nuclepore filters are convenient filters to study because their simple geometry can easily be modelled as an arrangement of parallel, cylindrical, uniform diameter, equidistant pores. This model of a filter pore was

---

[1]This efficiency curve has been taken from Hatch and Gross (2), and is credited to the Office of Health and Safety of the United States Atomic Energy Commission.

[2]The collection efficiency is defined as the ratio of collected particles to incident particles, and is typically a function of particle size and velocity.

[3]"Nuclepore" is a trade name of the Nuclepore Corporation, Pleasanton, California.

BEGIN LAST LINE OF TEXT HERE
BOTTOM OF IMAGE AREA OUTSIDE DIMENSION FOR PAGE NO. AND ILLUSTRATIONS
3/8"
PAGE NUMBER
EPA-287 (Cin.) (4-76)

proposed by Spurny and Pich (3), and was referred to as the "capillary" model of a filter[1]. Nuclepore filters are manufactured by bombarding sheets of polycarbonate with a collimated beam of fission fragments from a nuclear reaction. The fragments leave tracks of damaged material which, when chemically etched, form uniform cylindrical pores, perpendicular to the filter surface. The main difference between the filter and the model is the random pore spacing of the actual filter. For the larger pore diameter Nuclepore filters considered in the present study, there are approximately 10^5 pores per square centimeter of the filter area. Therefore it is reasonable to consider the filter to be characterized by an average porosity[2] from which an average pore spacing can be determined.

REVIEW OF PREVIOUS WORK

A widely used formula for predicting the inertial deposition of particles onto a capillary modelled filter was developed by Pich (4) to approximate the deposition of particles onto membrane[3] filters. The capillary model was a crude approximation to the sponge-like structure of membrane filters; and thereforeit was only necessary to obtain a crude solution to the flow field through the model pore. To simplify the solution, Pich assumed parabolic shapes for the streamlines. This assumption resulted in the erroneous situation of a constant axial component of the fluid velocity converging into the pore. Pich then applied Stokes' drag forces to obtain the equations of motion of a particle in the assumed flow field; and obtained a closed form solution to the equations of motion to determine the particle trajectory and impaction[4] efficiency. The crude assumptions in this theory became more critical when it was applied to the study of Nuclepore filters, whose structure is closely approximated by the capillary model. These shortcomings of Pich's theory have been noted and discussed by Smutek and Pich (5), and

---

[1]This is a good title for a model of sub-micron pore diameter filters, but it is misleading in reference to large pore filters whose pore length to diameter ratio is near unity. However the model is the same in either case, and it has been convenient to conform to the terminology used by Spurny and Pich.

[2]Filter porosity is defined as the fraction of total filter volume that is occupied by porous space. For Nuclepore filters, the porosity is simply the ratio of the total pore area to the total area of the filter (including the pores).

[3]Here "membrane" filters are meant to imply the filters typified by the Millipore Corporation cellulose filters.

[4]Inertial deposition is often referred to as inertial impaction, or simply impaction. These terms have been used interchangeably in this work.

BEGIN FIRST LINE OF TEXT HERE
TYPING GUIDE SHEET
CENTER OF PAGE
TOP OF IMAGE AREA
DROPPED HEAD; BEGIN SECTIONS HERE

by Smith and Phillips (6). Smutek and Pich developed an improved theory by considering an approximation to the flow field which took into account the increasing axial velocity into the pore. However in order to obtain a relatively simple closed form solution to the problem, they were still forced to make basic simplifications of the flow field model. These simplifications have been thoroughly discussed by Smutek and Pich, with the conclusion that their simplified flow model only gives reliable estimates of the impaction efficiency for "high porosity" filters.

Spurny, et al. (7) have conducted an extensive investigation of the Nuclepore filter. They considered the collection of particles to be the result of three primary mechanisms: inertial impaction, interception, and diffusion. Electrostatic, gravitational, thermal, and other secondary forces were neglected. Pich's original formula was used to determine the partial efficiency due to inertial impaction. The partial efficiency due to interception was added to account for the deposition of particles whose center of mass trajectory passed within one particle radius of the filter. This term had to be modified by an empirical weighting factor to obtain agreement between theory and experiment. Their work was primarily restricted to the sub-micron range of particle and pore diameters. In this region, the diffusion term was relatively large, and the inaccuracies in Pich's theory may not have been too serious. They also restricted themselves to cases with small interception terms. Spurny and Madelaine (8) have considered this latter restriction, and have proposed an empirical weighting factor which is a function of the particle/pore radius ratio. This allows them to treat problems with larger interception terms, but does not reduce the inaccuracies in Pich's formula.

Smith and Phillips (6) have recently solved for the combined impaction and interception efficiencies by a numerical relaxation technique. They solved for a specific porosity (11.1%), a specific pore diameter (1.0μm), and a specific approach velocity (1.0 m/sec). A similar numerical approach has been conducted independently in the present work.

PRESENT WORK

The present study is concerned with large[1] pore Nuclepore filters, and particles whose diameters are greater than 1μm. The experimental work has been conducted with a 9.5μm pore diameter Nuclepore filter, having a porosity of approximately 10%. For this case, the partial efficiency of diffusion is less than one tenth of one percent[2]. Therefore diffusion is

---

[1]The pores are assumed to be large enough to enable the assumption of continuum flow through the pore. This is discussed later in this section.

[2]The partial efficiency of diffusion was calculated for a particle diameter of 1μm, from the equation presented by Spurny, et al. (7), and attributed to Gormley and Kennedy (9).

BEGIN LAST LINE OF TEXT HERE
BOTTOM OF IMAGE AREA OUTSIDE DIMENSION FOR TABLES AND ILLUSTRATIONS
3/8"
PAGE NUMBER
EPA-287 (Cin.) (4-76)

BEGIN FIRST LINE OF TEXT HERE
TYPING GUIDE SHEET
CENTER OF PAGE
TOP OF IMAGE AREA
DROPPED HEAD; BEGIN SECTIONS HERE

negligible, and inertial impaction and interception are the critical mechanisms for deposition. Pich's early formula was unsuitable for this study because the flow model was too crude. The recent works of Smutek and Pich (5) and Smith and Phillips (6) were not available when this work was begun. An approach similar to that used by Smith and Phillips has been followed.

Rather than attempt to solve for the flow field in closed form, a solution to the Navier-Stokes equations for flow through a circular pore was obtained numerically on a digital computer. The equations of motion for a particle in the flow field were then solved numerically to obtain a particle trajectory. The critical trajectory for impaction to occur was found by a trial and error iteration. Assuming a uniform concentration of particles upstream of the filter, the impaction efficiency could be determined from the critical trajectory. By considering a particle to impact whenever its trajectory came within a particle radius of the filter surface, it was possible to combine the effects of impaction and interception, and thus avoid the need for an empirical weighting factor.

In the present study, the flow through the pore has been assumed to be in the continuum flow regime. The flow around the particle has been assumed to be Stokes' flow modified by the Cunningham correction for slip. Continuum flow is generally characterized by a Knudsen number much less than unity. For a 9.5μm pore diameter, and a mean free path for air molecules, $\lambda = 0.065\mu m$, the Knudsen number is given as

$$Kn = \frac{\lambda}{R_{pore}} = 0.0137 << 1$$

Similarly the Knudsen number for a 1μm diameter particle is

$$Kn = \frac{\lambda}{R_{part}} = 0.13 < 1$$

Since the Knudsen number for a 1μm particle is not greatly less than one, the inertial parameter in the equations of motion for the particle has been multiplied by the Cunningham slip correction factor[1].

The flow field through a plexiglas model of the filter was studied experimentally using a glycerin-water mixture, and a flow visualization technique which used dye injection to trace experimental streamlines. The streamlines were photographed and found to compare favorably with the streamlines obtained from the theoretical flow field solutions.

---

[1]The form of the Cunningham slip correction factor used in this work has been presented by Stern, et al. (10), and was based on Millikan's (11) data.

BEGIN LAST LINE OF TEXT
BOTTOM OF IMAGE AREA, OUTSIDE DIMENSION FOR TABLES AND ILLUSTRATIONS
3/8"

PAGE NUMBER
EPA-287 (Cln.)
(4-76)

BEGIN FIRST LINE OF TEXT HERE
TYPING GUIDE SHEET
CENTER OF PAGE
TOP OF IMAGE AREA
DROPPED HEAD: BEGIN SECTIONS HERE
6-1/2"
9-1/8"
BEGIN LAST LINE OF TEXT
3/8"
BOTTOM OF IMAGE AREA. OUTSIDE DIMENSION FOR TABLES AND ILLUSTRATIONS
PAGE NUMBER
EPA-287 (Cin-)
(4-76)

Experimental collection efficiencies have been obtained for a 9.5μm pore diameter Nuclepore filter, and particle diameters ranging from 1 to 9μm. The particles were generated with a Berglund-Liu monodisperse aerosol generator, and the filter was analyzed using an optical fluorescence technique. The experimental efficiencies compared quite favorably with the model in the case of a liquid aerosol but fell well below the predictions of the model in the case of a solid aerosol.

The computer model has been applied to study the effect of certain parameters upon the curve of impaction efficiency versus particle diameter. The parameters considered were: the pore Reynolds number (and therefore the air flow rate through the filter), the particle density, the filter thickness, and the filter porosity.

* BEGIN FIRST LINE OF TEXT HERE
CENTER OF PAGE
TOP OF IMAGE AREA
DROPPED HEAD: BEGIN SECTIONS HERE

SECTION 2

CONCLUSIONS

The intent of this study has been to develop and validate a theoretical procedure for predicting the collection efficiency of large pore Nuclepore filters and to explore their use as a particle fractionator. A theoretical procedure has been developed and validated which predicts the impaction efficiency of the filter. The experimental results which validate the impaction theory show that particles which impact upon the filter surface are not necessarily captured by the surface. For this reason, the theory is not yet one of collection efficiency. The impaction theory will, however, become a collection theory with the development of an adequate theory or mechanism for particle capture. It seems unlikely that the answer to this problem lies with being able to predict the probability of capture for a given particle so much as being able to devleop a reliable mechanism for particle capture. Cahill, et al. (12) report qualitative success with enhancing the collection efficiency of large pore Nuclepore filters by means of a grease base sticking agent applied to the filter surface. They report that such precoated filters are now commercially available from Nuclepore Corporation. If such techniques can be developed to the point where, within the accuracy demanded of the sampling results, all particles impacting upon the filter surface are captured, then the theory presented here becomes a theory which quite accurately predicts collection efficiency.

A comparison of the present work with earlier theories is seen in Figure 1. The predictions of earlier theories presented by Spurny, et al. (7), Spurny and Madelaine (8), and Smutek and Pich (5) are compared with the present theory. The differences between the present theories were based upon an approximate flow field which enabled a closed form solution. The present work is based upon a numerical solution of the Navier-Stokes equations. The present theory also combines the effects of inertia and interception within a single efficiency and is, therefore, a more fundamental solution to the same problem originally set up by Pich (4) and Spurny and Pich (3).

The theory has been applied to study the effects of pore Reynolds number, particle density, filter thickness, and filter porosity. It is concluded that relatively small variations in filter thickness and porosity do not significantly alter the impaction efficiency of the filter. The Reynolds number can be controlled by varying the face velocity of the filter. By varying the face velocity from about 40 cm/s to]0 cm/s, it is possible

BEGIN LAST LINE OF TEXT
BOTTOM OF IMAGE AREA. OUTSIDE DIMENSION FOR TABLES AND ILLUSTRATIONS
3/8"

PAGE NUMBER
EPA Form 2350-4 (4-80)
[PREVIOUSLY CIN. EPA FORM 2327]
TYPING GUIDE SHEET

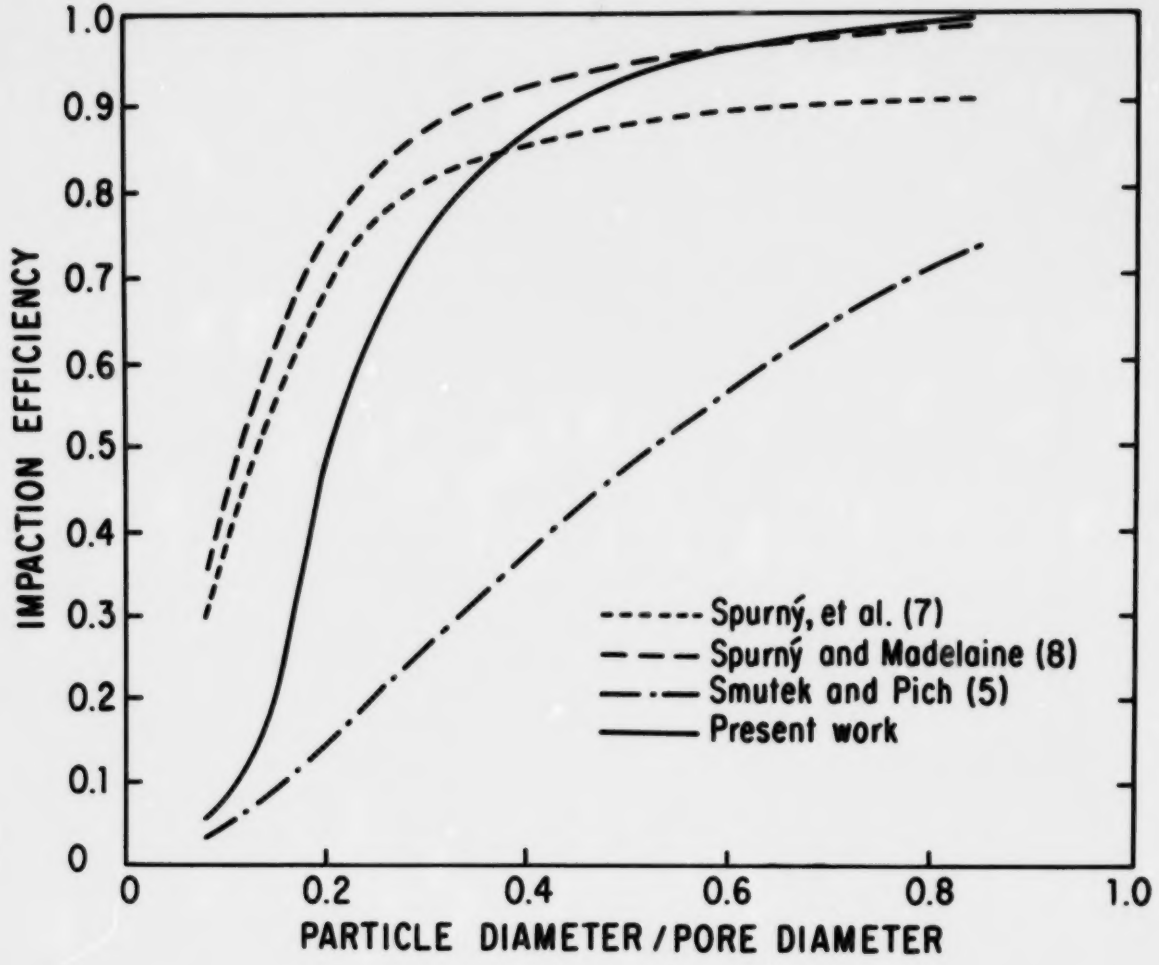

Figure 1. Present work compared to earlier theories. Re = 2, P = 10%, T = D_{pore}, ρ_p = 1.21 g/cm^3.

BEGIN FIRST LINE OF TEXT HERE
TYPING GUIDE SHEET
CENTER OF PAGE
TOP OF IMAGE AREA
DROPPED HEAD: BEGIN SECTIONS HERE
6-1/2"
8-1/8"
BEGIN LAST LINE OF TEXT
BOTTOM OF IMAGE AREA OUTSIDE DIMENSION FOR TABLES AND ILLUSTRATIONS
3/8"
PAGE NUMBER
EPA-287 (Cin.)
(4-76)

to adjust the 50 percent cut point between the desired limits of 2μm to 3.5μm. These figures assume spherical particles of unit density and a 12μm pore diameter Nuclepore filter with a porosity of 10 percent.

The present work is based upon the assumption of continuum flow. This assumption places a lower limit on any significant dimension (pore diameter or particle diameter) of approximately 1μm. The theory could be extended beyond this limit into the sub-micron region by introducing the concept of slip-flow. No attempt has been made to ascertain how far into the sub-micron region such an assumption would be valid. It is also clear that as one moves into the sub-micron region secondary effects such as diffusion which have been neglected in the present theory will become significant.

BEGIN FIRST LINE OF TEXT HERE
TYPING GUIDE SHEET
CENTER OF PAGE
TOP OF IMAGE AREA
DROPPED HEAD; BEGIN SECTIONS HERE

SECTION 3

FLOW FIELD THROUGH A CIRCULAR PORE

INTRODUCTION

Before one can determine the trajectories of particles in the vicinity of a filter pore, the flow field through the pore must be known. The flow field, in terms of the stream function field, has been determined by a numerical solution to the Navier-Stokes equations for flow through a circular pore. A finite difference method similar to that employed by Vrentas, et al. (13,14) has been used. The solution was programmed on the IBM 370/165 computer located at the Triangle Universities Computation Center in Research Triangle Park, North Carolina. The solutions were in the form of stream function values at a finite number of grid points. From the stream function values, it was possible either to interpolate for individual streamlines, or to determine the axial and radial velocity fields necessary for the calculation of particle trajectories.

To gain confidence in the theoretical flow field solution, a flow visualization technique was employed. A glycerin-water mixture, flowing through a porous plexiglas plate, was used to model the low Reynolds number flow through the filter pore. Dye was injected into the flow stream to trace streamlines, which were then photographed and compared to the theoretical streamlines.

THEORY

The present model of the flow field considers the flow through a circular pore to be a sudden contraction into the pore, followed by a sudden expansion out of the pore, as illustrated in Figure 2. The pore is a circular cylindrical hole of radius R_1, extending in the axial direction from $z = -z_0$ to $z = +z_0$. The flow outside the pore is confined within a hypothetical stream tube of radius R_2, extending to $z = \pm\infty$. R_2 is defined such that the pore/tube area ratio, $\left(\frac{\pi R_1^2}{\pi R_2^2}\right)$, is equal to the filter porosity, P. Thus the geometric parameter, $\beta = R_2/R_1$, is related to the filter porosity through the expression

$$P = \frac{1}{\beta^2} \qquad (3\text{-}1)$$

BEGIN LAST LINE OF TEXT
BOTTOM OF IMAGE AREA; OUTSIDE DIMENSION FOR TABLES AND ILLUSTRATIONS
3/8"

PAGE NUMBER
EPA-287 (Cln.) (4-76)

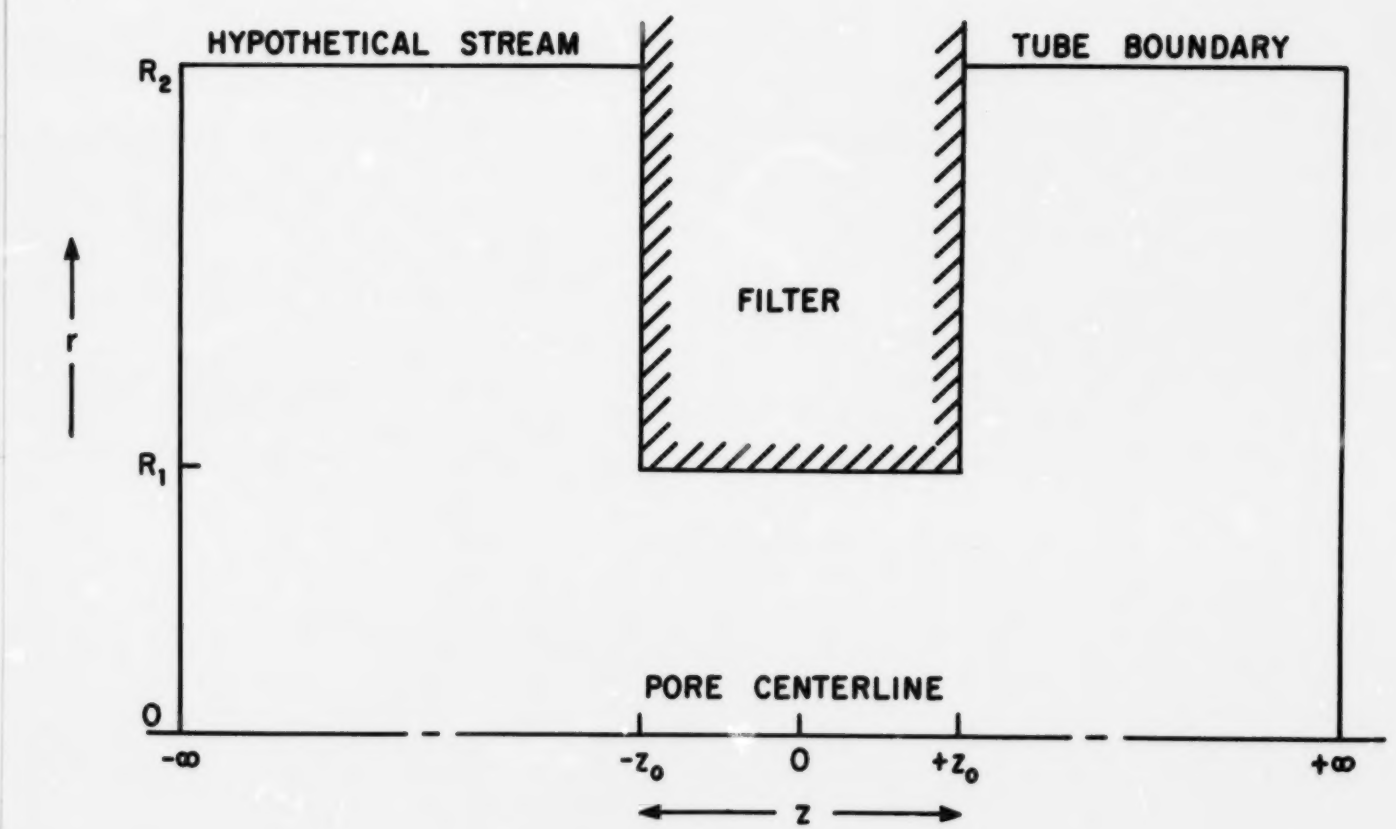

Figure 2. Theoretical model of a circular pore.

BEGIN FIRST LINE OF TEXT HERE
TYPING GUIDE SHEET
CENTER OF PAGE
TOP OF IMAGE AREA
DROPPED HEAD: BEGIN SECTIONS HERE
6-1/2"
3/8"
BEGIN LAST LINE OF TEXT
BOTTOM OF IMAGE AREA, OUTSIDE DIMENSION FOR TABLES AND ILLUSTRATIONS
PAGE NUMBER
EPA-287 (Cin.) (4-76)

A non-slip boundary condition has been imposed on the filter surfaces. Along the pore centerline and along the hypothetical tube wall, a condition of zero radial velocity and zero shear stress has been used. The flow at $z = \pm\infty$ is uniform parallel flow in the axial direction, with $v_z = U_\infty$.

The flow has been considered to be axially symmetric, with zero velocity and zero gradients in the ϕ direction. Furthermore, the flow has been considered to be steady state, isothermal, laminar flow of an incompressible, Newtonian fluid with constant viscosity. For the case of air flow through the filter pore, body forces have been neglected, and therefore the orientation of the filter with respect to gravity is unimportant. However gravity forces are important with the glycerin-water flow visualization model. For this reason, the flow field solution has been developed for the more general case of a vertical cylinder (pore) with the gravity term incorporated into the pressure gradient. Thus let the effective pressure, p, be related to the gravity force, F_2, and the actual pressure, p', through expression

$$p = zF_z - p' \tag{3-2}$$

Then the axial and radial pressure gradients may be expressed

$$\frac{\partial p}{\partial z} = F_z - \frac{\partial p'}{\partial z} \tag{3-3}$$

$$\frac{\partial p}{\partial r} = - \frac{\partial p'}{\partial r} \tag{3-4}$$

For the above conditions, Schlichting (15) presents the Navier-Stokes equations, in cylindrical coordinates, as

$$\rho_f \left(v_r \frac{\partial v_r}{\partial r} + v_z \frac{\partial v_r}{\partial z} \right) = - \frac{\partial p}{\partial r} + \mu_f \left(\frac{\partial^2 v_r}{\partial r^2} + \frac{1}{r} \frac{\partial v_r}{\partial r} - \frac{v_r}{r^2} + \frac{\partial^2 v_r}{\partial z^2} \right) \tag{3-5}$$

$$\rho_f \left(v_r \frac{\partial v_z}{\partial r} + v_z \frac{\partial v_z}{\partial z} \right) = - \frac{\partial p}{\partial z} + \mu_f \left(\frac{\partial^2 v_z}{\partial r^2} + \frac{1}{r} \frac{\partial v_z}{\partial r} + \frac{\partial^2 v_z}{\partial z^2} \right) \tag{3-6}$$

with the continuity equation,

$$\frac{\partial v_r}{\partial r} + \frac{v_r}{r} + \frac{\partial v_z}{\partial z} = 0 \tag{3-7}$$

Making the following substitutions,

BEGIN FIRST LINE OF TEXT HERE
TYPING GUIDE SHEET
CENTER OF PAGE
TOP OF IMAGE AREA
DROPPED HEAD: BEGIN SECTIONS HERE

$$V = \frac{v_r}{U_1}$$

$$U = \frac{v_z}{U_1} \qquad (3\text{-}8)$$

$$R = \frac{r}{R_1}$$

$$Z = \frac{z}{R_1}$$

the Navier-Stokes equations may be non-dimensionalized to give

$$V \frac{\partial V}{\partial R} + U \frac{\partial V}{\partial Z} = - \frac{1}{\rho_f U_1^2} \frac{\partial p}{\partial R} + \frac{2}{Re} \left(\frac{\partial^2 V}{\partial R^2} + \frac{1}{R} \frac{\partial V}{\partial R} - \frac{V}{R^2} + \frac{\partial^2 V}{\partial Z^2} \right) \qquad (3\text{-}9)$$

$$V \frac{\partial U}{\partial R} + U \frac{\partial U}{\partial Z} = - \frac{1}{\rho_f U_1^2} \frac{\partial p}{\partial Z} + \frac{2}{Re} \left(\frac{\partial^2 U}{\partial R^2} + \frac{1}{R} \frac{\partial U}{\partial R} + \frac{\partial^2 U}{\partial Z^2} \right) \qquad (3\text{-}10)$$

$$\frac{\partial V}{\partial R} + \frac{V}{R} + \frac{\partial U}{\partial Z} = 0 \qquad (3\text{-}11)$$

The Reynolds number appears as the characteristic dimensionless parameter, defined

$$Re = \frac{2 R_1 U_1 \rho_f}{\mu_f} \qquad (3\text{-}12)$$

The pore radius and the average velocity through the pore have been used as the non-dimensionalizing parameters, R_1, and U_1. The boundary conditions for U and V are given in Figure 3.

The pressure terms were eliminated from equations (3-9) and (3-10) by first differentiating equation (3-9) with respect to Z, differentiating equation (3-10) with respect to R, and then subtracting the resulting two equations. The complicated form of the resulting equation, however, makes it inconvenient to solve. It was simplified in the usual manner by introducing the stream function, ψ .

BEGIN LAST LINE OF TEXT
BOTTOM OF IMAGE AREA, OUTSIDE DIMENSION FOR TABLES AND ILLUSTRATIONS
3/2"

EPA-287 (Clin.)
(4-76)

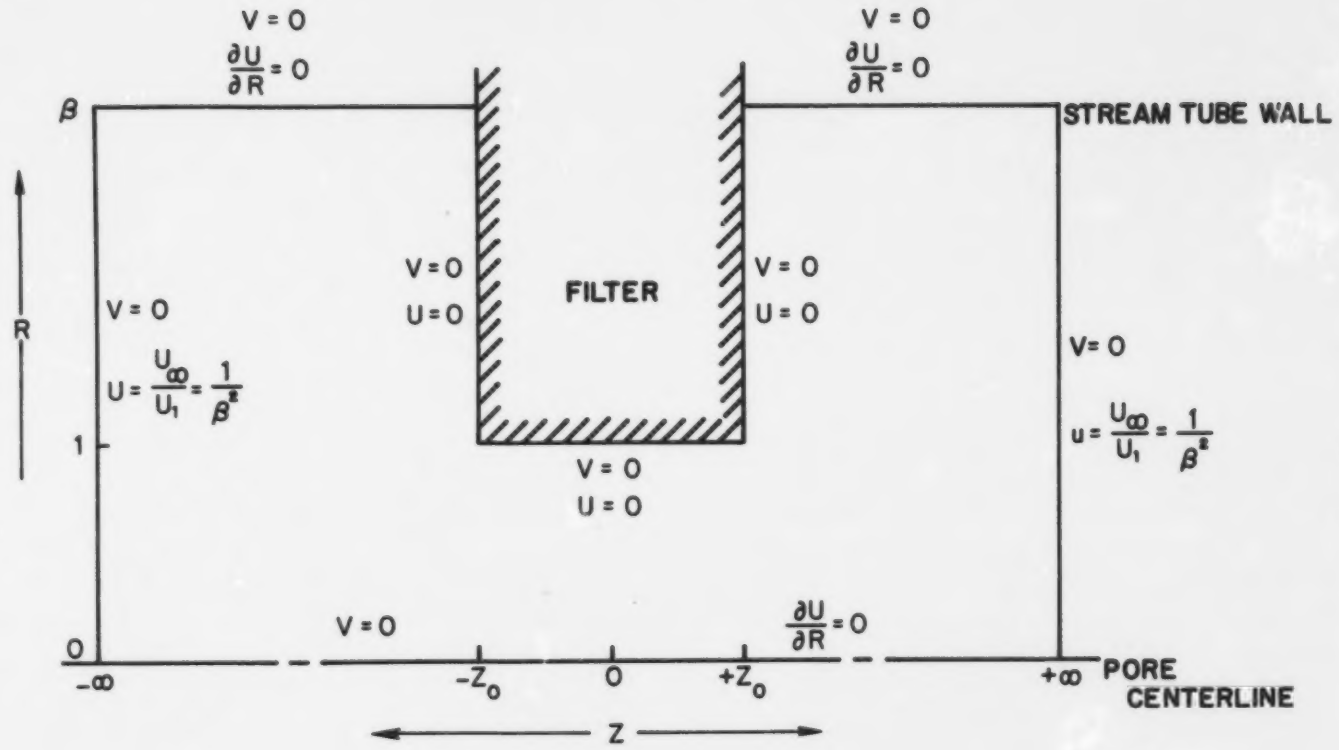

Figure 3. Boundary conditions on U and V in the R-Z coordinate system.

BEGIN FIRST LINE OF TEXT HERE
TYPING GUIDE SHEET
CENTER OF PAGE
TOP OF IMAGE AREA
DROPPED HEAD, BEGIN SECTIONS HERE

$$U = -\frac{1}{R}\frac{\partial \psi}{\partial R} \qquad (3\text{-}13)$$

$$V = \frac{1}{R}\frac{\partial \psi}{\partial Z} \qquad (3\text{-}14)$$

It should be noted that equations (3-13) and (3-14) satisfy the continuity equation (3-11) identically.

A further simplification was achieved by introducing the only non-zero component of the vorticity vector as

$$\omega = \omega_{\phi} = \frac{\partial V}{\partial Z} - \frac{\partial U}{\partial R} \qquad (3\text{-}15)$$

Substitution of equations (3-13), (3-14), and (3-15) into the equation resulting from the elimination of the pressure terms, and utilization of the continuity equation, give

$$\frac{\partial^2 \omega}{\partial Z^2} + \frac{\partial^2 \omega}{\partial R^2} + \frac{1}{R}\frac{\partial \omega}{\partial R} - \frac{\omega}{R^2} = \frac{Re}{2}\left(\frac{1}{R}\frac{\partial \psi}{\partial Z}\frac{\partial \omega}{\partial R} - \frac{1}{R}\frac{\partial \psi}{\partial R}\frac{\partial \omega}{\partial Z} - \frac{\omega}{R^2}\frac{\partial \psi}{\partial Z}\right) \qquad (3\text{-}16)$$

Equation (3-16) is often referred to as the vorticity transport equation. Vorticity is related to the stream function through equation (3-15), which may be written

$$\omega = \frac{1}{R}\frac{\partial^2 \psi}{\partial Z^2} + \frac{1}{R}\frac{\partial^2 \psi}{\partial R^2} - \frac{1}{R^2}\frac{\partial \omega}{\partial R} \qquad (3\text{-}17)$$

Equations (3-16) and (3-17) are coupled, nonlinear, elliptic partial differential equations. For a unique solution to exist, it is necessary to specify boundary conditions for both ψ and ω over the entire boundary. It was possible to generate boundary conditions for the infinite region composed of the upstream and downstream hypothetical stream tube, and the filter pore, by applying equations (3-13), (3-14), and (3-15) to the boundary conditions on U and V. The boundary conditions generated for ψ and ω are shown in Figure 4.

Because of the nonlinearity and complexity of equations (3-16) and (3-17), it is necessary to solve them numerically. It is not possible to solve elliptic equations with closed boundary conditions, for an infinite region, by numerical methods. Therefore, following a method similar to that used by Vrentas, et al. (13), the infinite Z region was mapped into two finite η regions, where, upstream of the filter,

BEGIN LAST LINE OF TEXT
BOTTOM OF IMAGE AREA OUTSIDE DIMENSION FOR TABLES AND ILLUSTRATIONS
3/8"

EPA-287 (Cin.) (4-76)

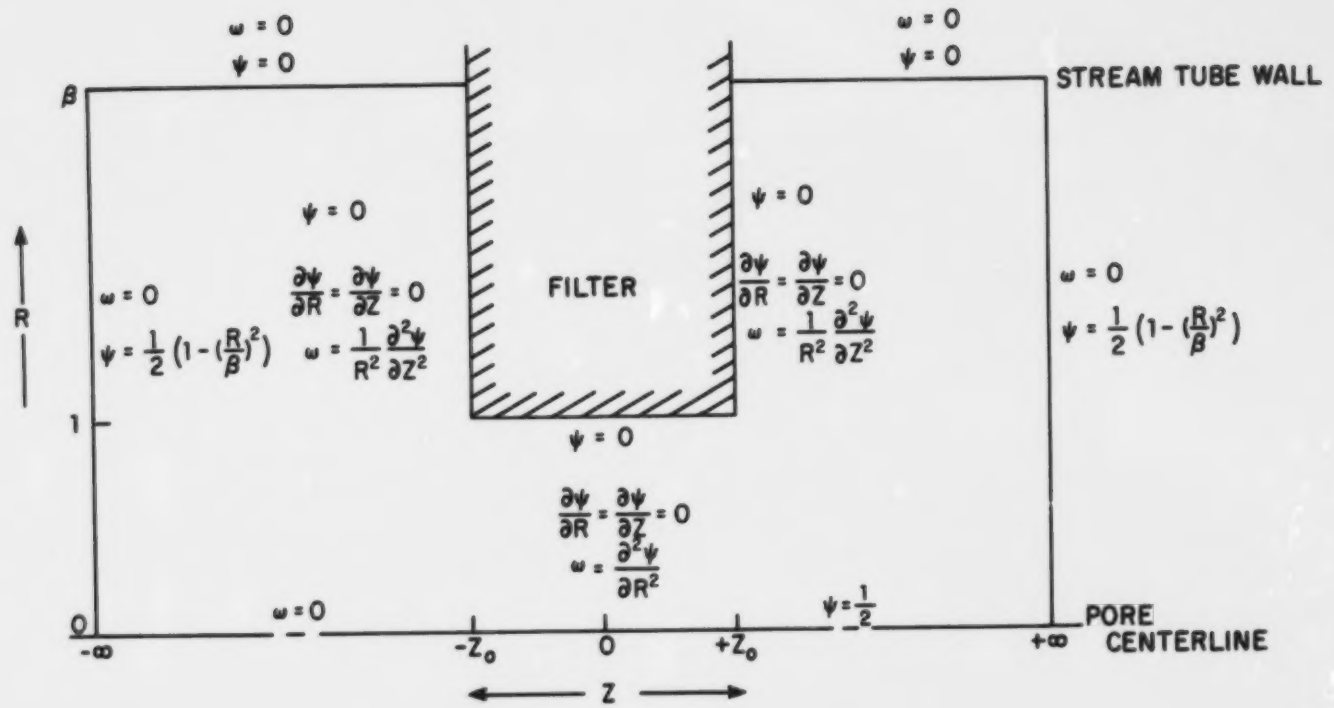

Figure 4. Boundary conditions on ψ and ω in the R-Z coordinate system.

BEGIN FIRST LINE OF TEXT HERE
TYPING GUIDE SHEET
CENTER OF PAGE
TOP OF IMAGE AREA
DROPPED HEAD; BEGIN SECTIONS HERE

$$\eta_u = \tanh\left(k_u(Z + Z_o)\right), \tag{3-18}$$

and downstream of the filter,

$$\eta_d = \tanh\left(k_d(Z - Z_o)\right). \tag{3-19}$$

The region within the pore was left in the original (R,Z) coordinate system. The constants k_u and k_d enabled the amplification of the regions near the pore entrance and exit, in order to account for relatively rapid changes in ψ and ω in these regions[1].

Substitution of $\eta = \tanh\ k(Z \pm Z_o)$ into equations (3-16) and (3-17) yields

$$X_1^2 \frac{\partial^2\omega}{\partial\eta^2} + X_2 \frac{\partial\omega}{\partial\eta} + \frac{\partial^2\omega}{\partial R^2} + \frac{1}{R}\frac{\partial\omega}{\partial R} - \frac{\omega}{R^2} = \frac{X_1 Re}{2}\left(\frac{1}{R}\frac{\partial\psi}{\partial\eta}\frac{\partial\omega}{\partial R} - \frac{1}{R}\frac{\partial\psi}{\partial R}\frac{\partial\omega}{\partial\eta} - \frac{\omega}{R^2}\frac{\partial\omega}{\partial\eta}\right) \tag{3-20}$$

$$\omega = \frac{X_1^2}{R}\frac{\partial^2\psi}{\partial\eta^2} + \frac{X_2}{R}\frac{\partial\psi}{\partial\eta} + \frac{1}{R}\frac{\partial^2\psi}{\partial R^2} - \frac{1}{R^2}\frac{\partial\psi}{\partial R} \tag{3-21}$$

where

$$X_1 = \frac{\partial\eta}{\partial Z} = k(1 - \eta^2) \tag{3-22}$$

$$X_2 = \frac{\partial X_1}{\partial Z} = X_1\frac{\partial X_1}{\partial\eta} = -2k^2\eta(1 - \eta^2) \tag{3-23}$$

Equations (3-20) and (3-21) apply both upstream and downstream if η and k are replaced by η_u and k_u, or η_d and k_d respectively. The boundary conditions for the three regions: upstream, pore, and downstream, are given in Figure 5.

NUMERICAL SOLUTION

Finite Difference Procedure

From equation (3-16) or (3-20), it can be seen that the relative size of the nonlinear terms is directly proportional to the Reynolds number.

---

[1]The transformation constants are discussed in more detail later in this section.

BEGIN LAST LINE OF TEXT HERE
BOTTOM OF IMAGE AREA, OUTSIDE DIMENSION FOR TABLES AND ILLUSTRATIONS

PAGE NUMBER
EPA-287 (Cin.) 14-76)

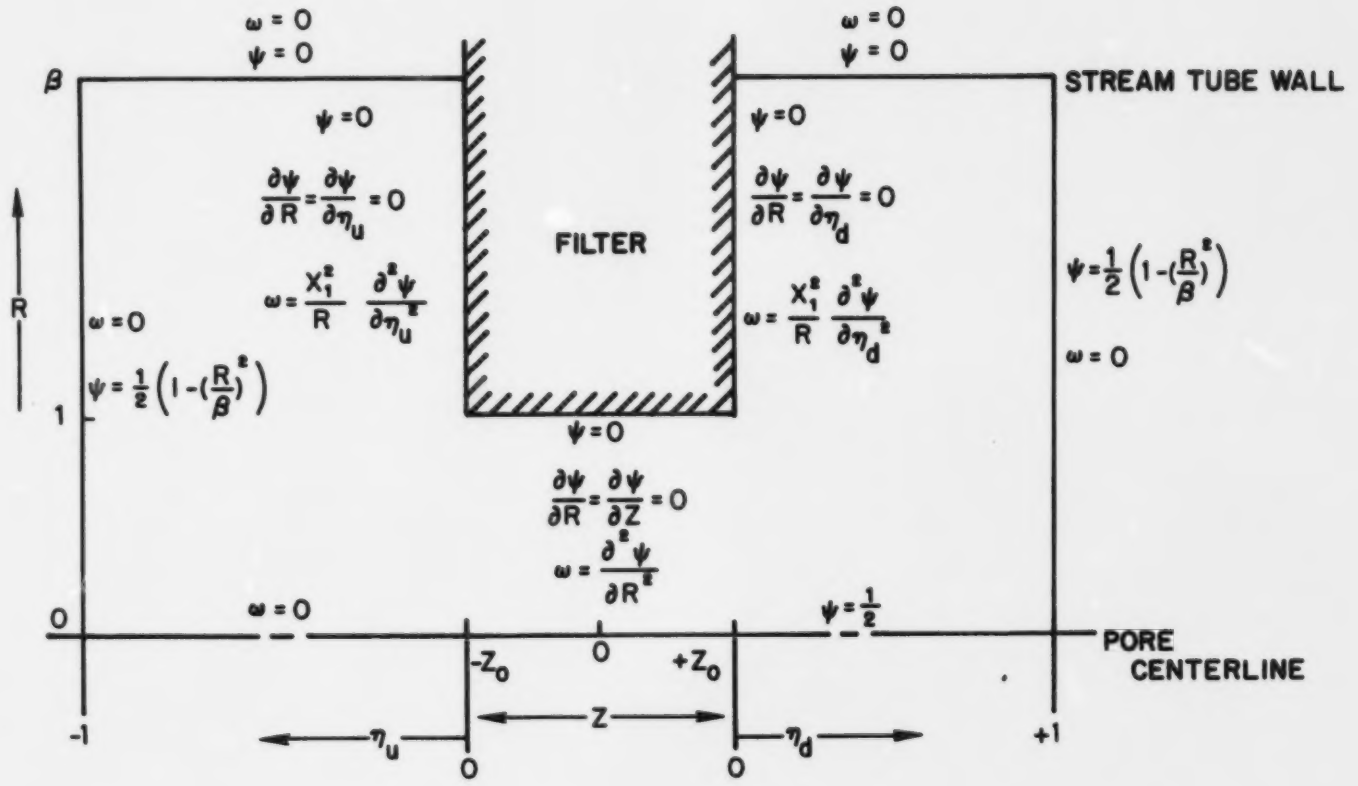

Figure 5. Boundary conditions on ψ and ω in the combined R-Z, R-η coordinate system.

BEGIN FIRST LINE OF TEXT HERE
TYPING GUIDE SHEET
CENTER OF PAGE
TOP OF IMAGE AREA
DROPPED HEAD: BEGIN SECTIONS HERE

For small Reynolds numbers, therefore, the nonlinearities will have a weak effect on the equations, and equations (3-16) and (3-17), or equations (3-20) and (3-21), can be solved satisfactorily by standard finite difference techniques. This involves approximating the derivatives by finite differences and substituting these approximations into the original differential equations to obtain difference equations. The finite difference derivative approximations were obtained from Taylor series expansions as presented by Forsythe and Wasow (16).

Solving equations (3-16) and (3-17), or equations (3-20) and (3-21), when in finite difference form, is equivalent to solving a system of simultaneous, nonlinear, algebraic equations. In the present work, the Gauss-Seidel iterative method was used. This involved breaking the region into finite difference grids and applying the difference equations at each grid point, always using the last available values for ψ and ω at the surrounding grid points. Repetitive sweeps of the grid matrix were made until the values of ψ and ω converged satisfactorily.

Because of the axial symmetry of the flow model, it was possible to use a rectangular grid network composed of uniformly spaced grids in the upstream, pore and downstream regions. Upstream the grid size was $(h_R x h_u)$. Inside the pore the grid size was $(h_R x h_Z)$. Downstream the grid size was $(h_R x h_d)$. In each of these regions, central difference approximations for uniformly spaced grids[1] were used to approximate the first and second derivatives of ψ and ω. The approximations were then used to derive the finite difference representation of the governing equations.

A problem was encountered at the pore entrance and exit. At the entrance, the central difference approximation had to be altered because the grid spacing changed from h_u to h_Z. This problem was dealt with by calculating $h_{Z_u} = \frac{1}{k_u} \tanh^{-1}(h_u)$, and using central difference approximations based upon variable grid spacings[1] to derive the difference form of equations (3-16) and (3-17). the pore exit was handled in a similar manner with $h_{Z_d} = \frac{1}{k_d} \tanh^{-1}(h_d)$.

A further problem was encountered at the last radial grid, adjacent to the hypothetical stream tube wall. A uniform radial grid spacing h_R, was used up to the last radial grid, and its value was set so as to ensure that a grid line coincided with the pore wall. Then a variable grid spacing,

---

[1]The central difference approximations have been taken from Forsythe and Wasow (16), and are presented here in Appendix A.

BEGIN LAST LINE OF TEXT
BOTTOM OF IMAGE AREA, OUTSIDE DIMENSION FOR TABLES AND ILLUSTRATIONS
3/8"

EPA-287 (Cont.)
(4-70)

BEGIN FIRST LINE OF TEXT HERE
TYPING GUIDE SHEET
CENTER OF PAGE
TOP OF IMAGE AREA
DROPPED HEAD: BEGIN SECTIONS HERE

dn, was used for the last radial grid to allow for the consideration of any desired filter porosity. Therefore central difference approximations with variable grid spacings in the radial direction were used on the last but one radial grid line (row), directly below the tube wall. The grid spacings for the various regions are illustrated in Figure 6.

In all regions, the finite difference representation of equations (3-16) and (3-17), or equations (3-20) and (3-21), at any internal grid point, (i,j), take the form

$$\omega_{i,j} = C_o \left(C_1\omega_{i,j+1} + C_2\omega_{i,j-1} + C_3\omega_{i+1,j} + C_4\omega_{i-1,j} \right) \qquad (3\text{-}24)$$

$$\psi_{i,j} = D_o \left(D_1\psi_{i,j+1} + D_2\psi_{i,j-1} + D_3\psi_{i+1,j} + D_4\psi_{i-1,j} - \omega_{i,j} \right) \qquad (3\text{-}25)$$

The coefficients vary for each region, and are quite complicated. The C_i are functions of ψ, and both the C_i and the D_i are functions of the independent variables, transformation constants, and Reynolds number. The coefficients for each region are presented in Appendix A.

For a given configuration, the boundary conditions enter as constants with the exception of the vorticity on the filter surfaces. To obtain a boundary condition for ω on a filter surface with a normal direction, n, it was necessary to derive a finite difference expression for $\frac{\partial^2\psi}{\partial n^2}$, and apply equation (3-17). This was achieved, following the work of Vrentas, et al., by a Taylor series expansion, noting that on the filter surface, $\psi = \frac{\partial\psi}{\partial n} = 0$. The expression for the vorticity on the filter surface is

$$\omega_w = \frac{4\psi_{w-1}}{(\Delta n)^2} - \frac{\psi_{w-2}}{2(\Delta n)^2} \qquad (3\text{-}26)$$

where w means the filter wall, and w-1, w-2, are values one and two grids away from the wall. This expression is derived in Appendix A. The vorticity at each corner of the pore was obtained by taking an average of the vorticity approximated in each normal direction.

The step by step solution for the flow field may be summarized as follows:

1. A two-dimensional finite difference grid network was set up as shown in Figure 6.

BEGIN LAST LINE OF TEXT
BOTTOM OF IMAGE AREA, OUTSIDE DIMENSION FOR TABLES AND ILLUSTRATIONS
3/8"

EPA-287 (Cin.)
(4-76)

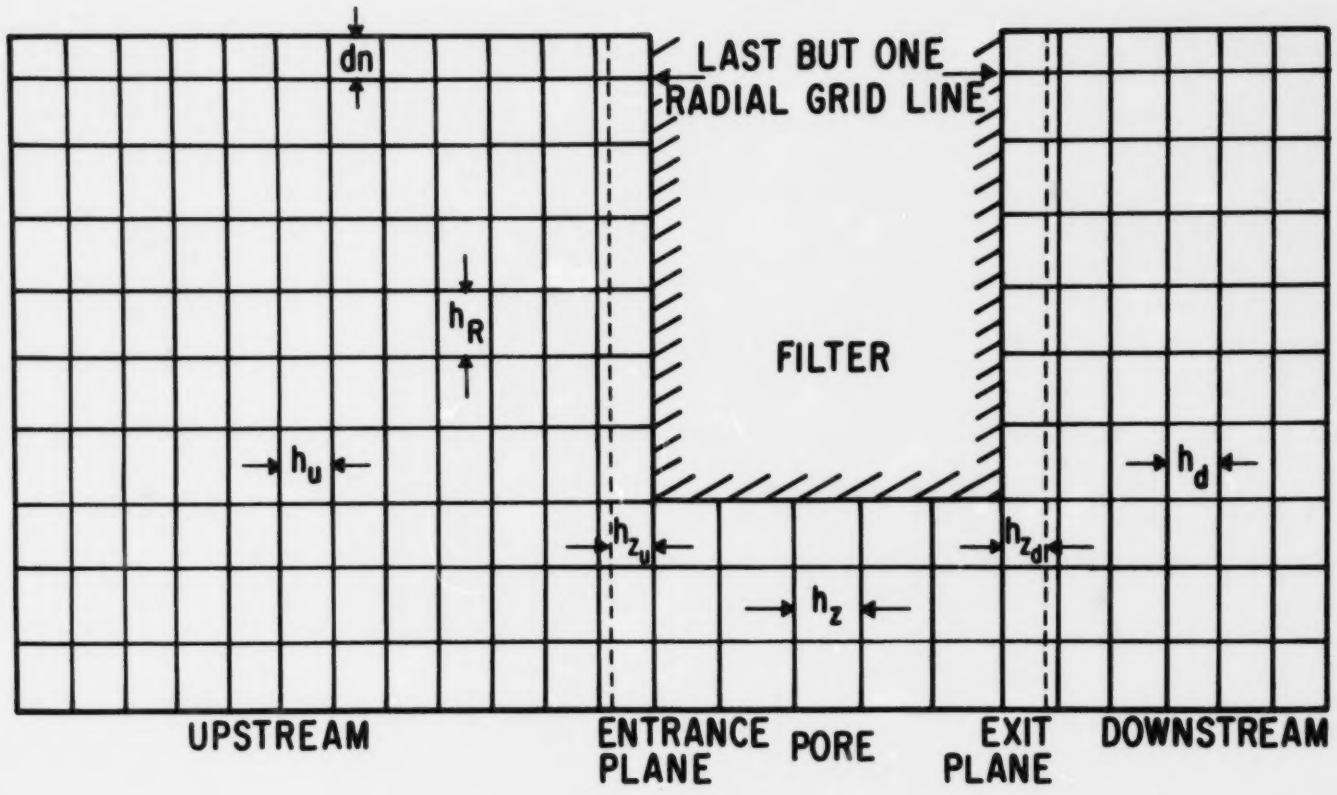

Figure 6. Finite difference grid network

BEGIN FIRST LINE OF TEXT HERE
TYPING GUIDE SHEET
CENTER OF PAGE
TOP OF IMAGE AREA
DROPPED HEAD; BEGIN SECTIONS HERE

2. Initial values were assumed at all points, and the constant boundary conditions were set as presented in Figure 5.

3. The finite difference form of equation (3-17) or (3-21), given by equation (3-25) together with the appropriate coefficients, was applied at an interior grid point to obtain a new value of ψ at this point, assuming ω to be known. The new value of ψ was compared to its previous value as a test for convergence at this point.

4. The value of ω on the filter surface was updated by equation (3-26) if necessary. The new value of ω was compared to its previous value as a test for convergence at this point.

5. The finite difference form of equation (3-16) or (3-20), given by equation (3-24) together with the appropriate coefficients, was applied at an interior grid point to obtain a new value of ω at this point, assuming ω to be known. The new value of ω was compared to its previous value as a test for convergence at this point.

6. Steps 3, 4, and 5 were repeated at the next grid point. In all calculations, the most recently available values for ψ and ω were used. This operation was repeated until one column by column sweep of the grid matrix had been completed.

7. After each sweep of the grid matrix, a test was conducted to determine whether or not the values of ψ and ω had converged sufficiently at every grid point in the network. The values of ψ and ω were considered to have converged when they had not changed to five decimal places.

8. Repetitive sweeps of the grid network were performed until either convergence had been achieved, or the maximum allowable number of iterations had been exceeded. If the solution had converged, the values of ψ and ω, to five decimal places, were punched on computer cards.

Convergence of Numerical Solution

The flow field is given by the exact solution to equations (3-16) and (3-17), or equations (3-20) and (3-21), together with the appropriate boundary conditions. The computer solution to the difference equations, (3-24) and (3-25), is only an approximation to the exact flow field solution. The truncation error is the error inherent in the finite difference derivative approximations, and is due to the neglection of higher order terms in the Taylor series expansions[1]. This error is proportional to h^2 for uniformly spaced grids, and roughly proportional to h for nonuniform grids. Therefore the truncation error should decrease, and the numerical solution

[1] See Forsthe and Wasow (16), p. 184.

BEGIN LAST LINE OF TEXT
BOTTOM OF IMAGE AREA, OUTSIDE DIMENSION FOR TABLES AND ILLUSTRATIONS
3/8"

EPA-287 (Cin.) (4-76)

BEGIN FIRST LINE OF TEXT HERE
TYPING GUIDE SHEET
CENTER OF PAGE
TOP OF IMAGE AREA
DROPPED HEAD, BEGIN SECTIONS HERE

to the difference equations should approach the exact solution to the differential equations, as h approaches zero.

Figures 7 and 8 show the convergence of the stream function and the axial and radial velocities at a specific grid point. This point is the point nearest to the pore entrance corner, and in the pore entrance plane. There are three reasons why this point should be the most critical point at which to observe convergence. The difference equations are for nonuniform grid spacings in the pore entrance plane, and thus the truncation error is relatively larger there than elsewhere; the streamlines bend most sharply around the entrance corner; and the vorticity boundary condition is less accurate at the entrance corner because of the discontinuity in the normal derivative of the stream function. At this point, Figures 7 and 8 show that the stream function and the velocities are converging as the grid spacing approaches zero. The grid space, h_o, represents the smallest grid size used in this work. The data points shown were obtained from increasingly cruder grid size solutions of h_o, $2h_o$ and $4h_o$[1]. Although the stream function and velocity values have not completely converged, the amount of convergence may be considered to be satisfactory. This will be shown in SECTION 4, where it will be seen that further refinement of the grid size would not greatly affect the curve of impaction efficiency versus particle diameter.

The computer program used to determine the flow field through a filter pore for a given Reynolds number, filter thickness, and filter porosity, is discussed and presented in detail by Parker (17).

RESULTS OF THE FLOW FIELD SOLUTION

The flow field solutions are presented as families of streamlines for pore Reynolds numbers of 1, 2, and 3, in Figures 9, 10, and 11. In all cases, the porosity was 10%, and the filter thickness was equal to the pore diameter. The upstream and downstream transformation constants, k_u and k_d, and the Reynolds number are related to the relative size of the nonlinear terms in equation (3-20). Furthermore, k_u and k_d controlled the upstream and downstream expansion of the grid spacing in Z-space. For these reasons, the values of k_u and k_d significantly affected the number of sweeps of the grid matrix necessary to obtain convergence for a given Reynolds number. Values of $k_u = 0.325$, and $k_d = 0.175$ were found to be satisfactory for $Re \leq 10$. However convergence problems occurred for $Re > 10$. In this study, the Reynolds numbers needed to give 50% cut-points in the desired range of 2μm to 3.5μm, for a 12μm pore diameter filter, were found to be about $Re \simeq 3$ and $Re = 1$, respectively. Therefore solutions for $Re > 10$ were not of interest.

---

[1]The actual number of axial and radial grids corresponding to h_o, is presented in SECTION 4.

BEGIN LAST LINE OF TEXT HERE
BOTTOM OF IMAGE AREA, OUTSIDE DIMENSION FOR TABLES AND ILLUSTRATIONS
3/8"

PAGE NUMBER
EPA-287 (Cin.) (4-76)

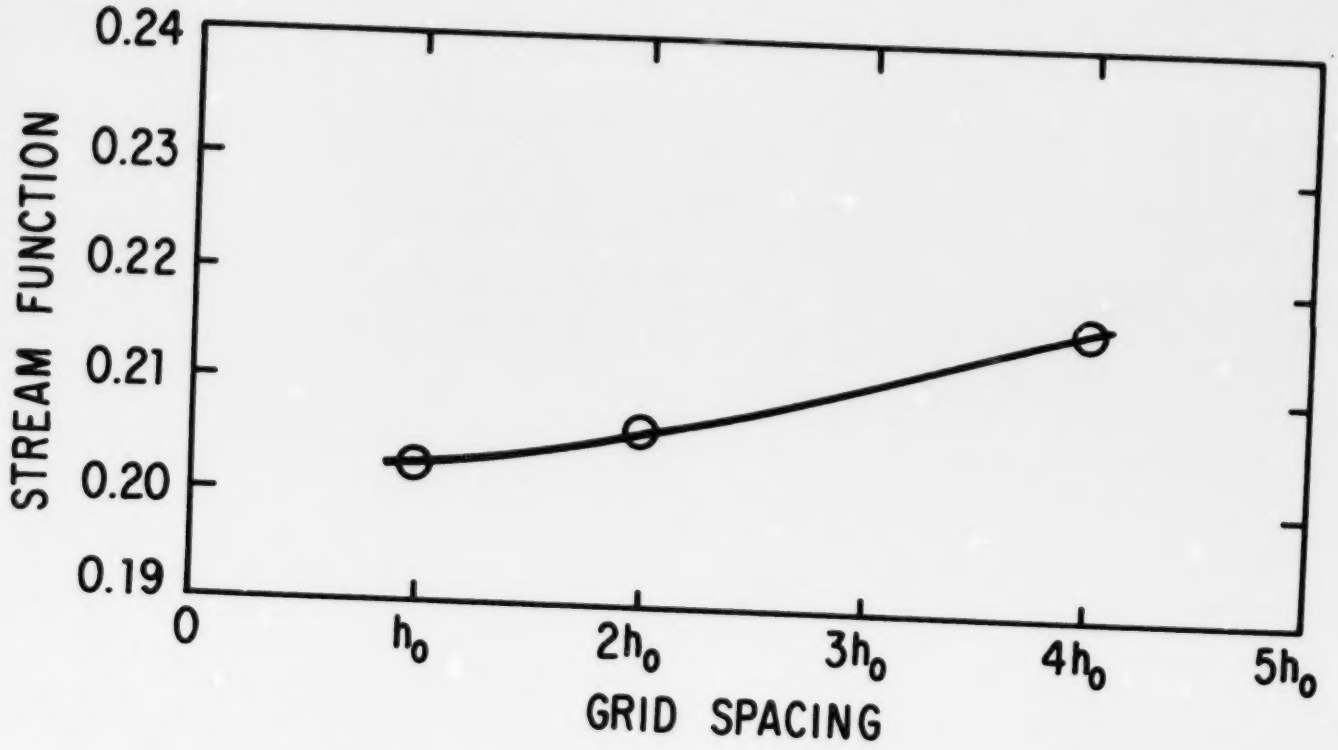

Figure 7. Convergence of the stream function at a point near the pore entrance corner as the grid spacing approaches zero. Re = 2, P = 10%, T = D_{pore}.

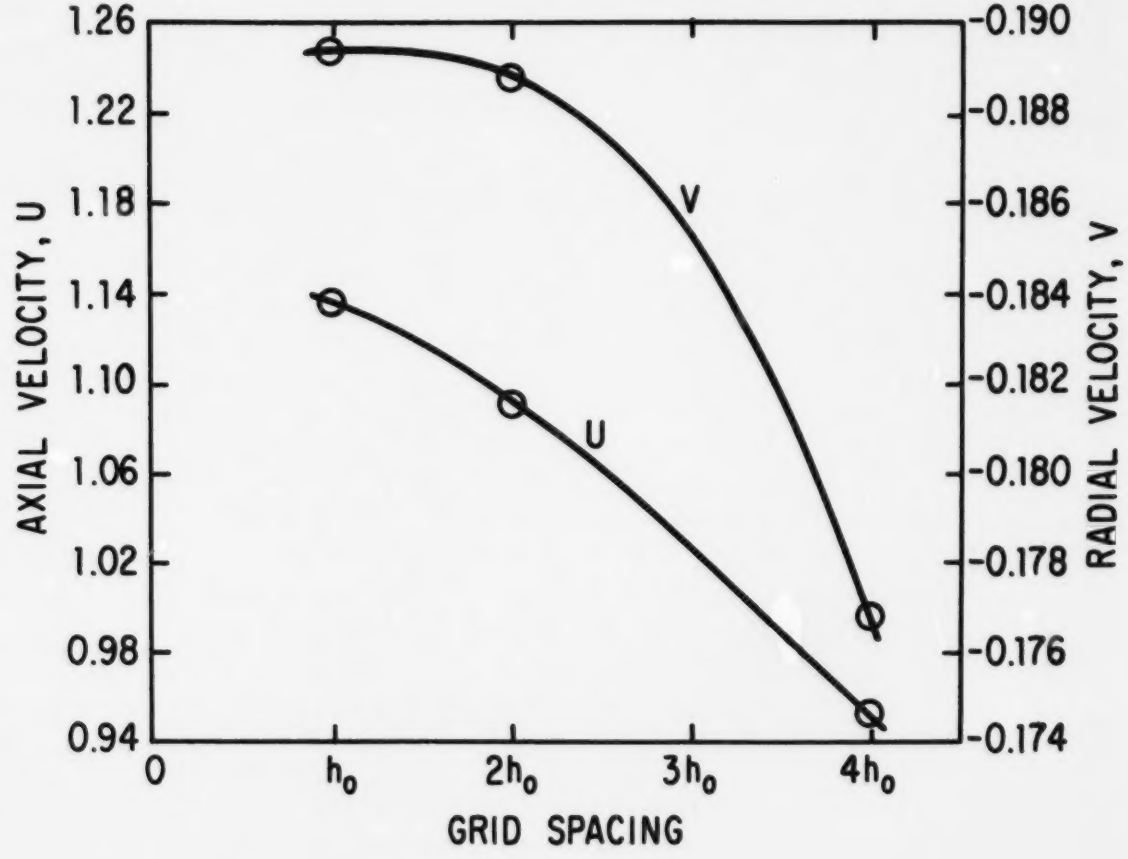

Figure 8. Convergence of U and V at a point near the pore entrance corner as the grid spacing approaches zero. R = 2, P = 10%, T = D_{pore}.

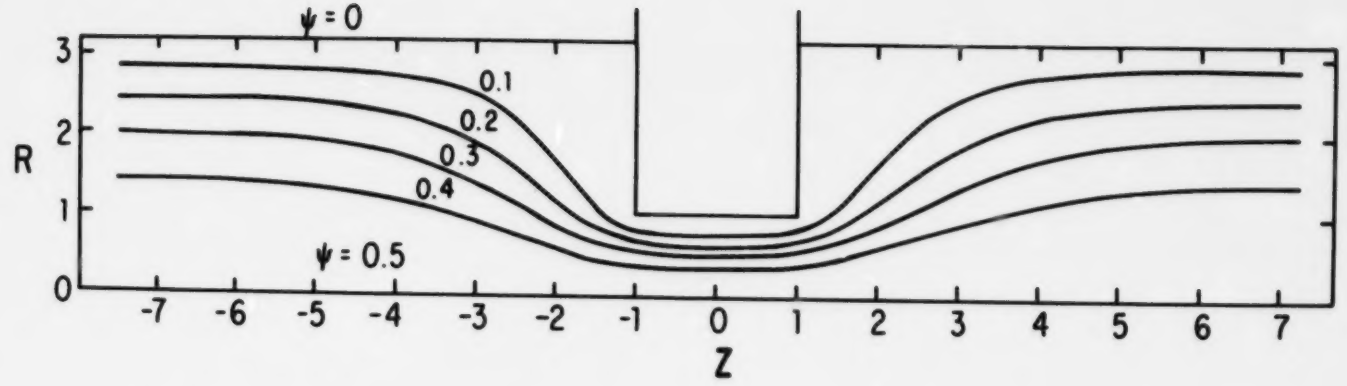

Figure 9. Streamlines through a circular pore Re = 1, P = 10%, T = D_{pore}.

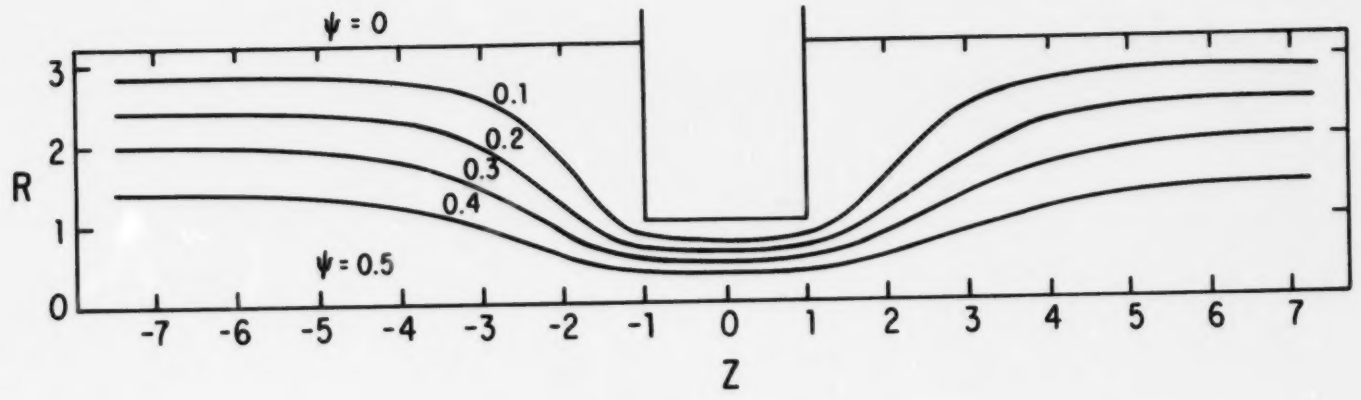

Figure 10. Streamlines through a circular pore Re = 2, P = 10%, T = D_{pore}.

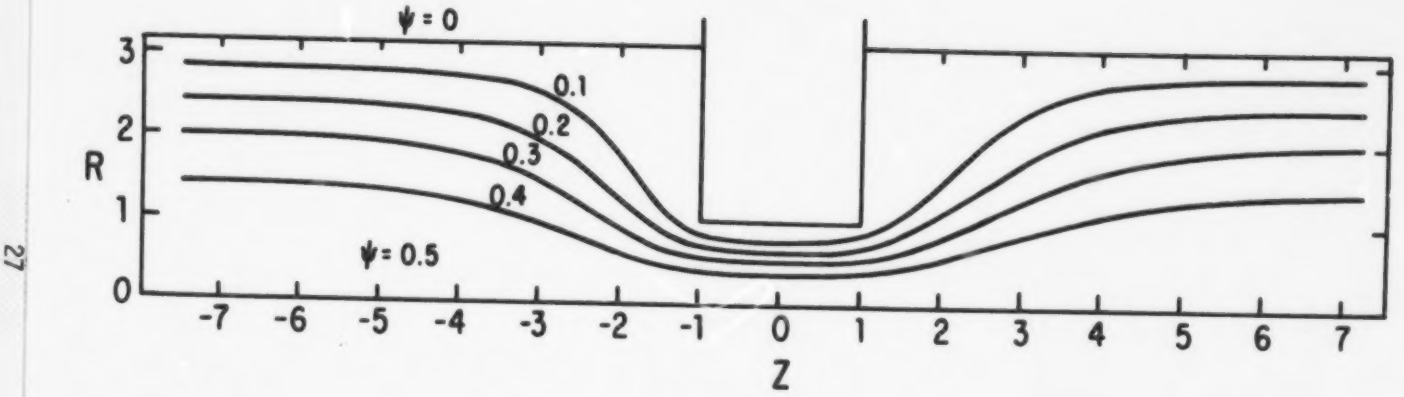

Figure 11. Streamlines through a circular pore Re = 3, P = 10%, T = D_{pore}.

Once the ψ and ω solutions had been obtained, the stream function field was used to obtain the axial and radial velocity fields in finite difference form, from equations (3-13) and (3-14). The velocity fields were then used as a basis for the trajectory calculations described in SECTION 4.

FLOW VISUALIZATION MODEL

A physical model of the flow field has been developed and used to obtain experimental streamlines through a pore. The low pore Reynolds number, characteristic of air flow through the filter pore, was obtained using a mixture of glycerin and water flowing through a porous plexiglas plate. It was desirable to keep the average Reynolds number less than Re = 10, because the computer solution begins to have convergence problems above Re = 10, and also the Reynolds numbers of most interest with the actual filter are Re = 1, 2, and 3. Reynolds numbers of 5 and 8 were as low as could be obtained[1]. They were obtained with a concentrated solution of about 87% by volume glycerin, and flow rates ranging from 1/4 to 1/2 ft^3/min. To ensure that this model would have the same flow pattern as air flowing through a filter pore, it was convenient to align the gravity forces vertically, so that they could be incorporated into the pressure terms and eliminated from the theoretical solution.

Experimental Setup

The apparatus used for the fluid flow field model is illustrated in Figure 12. The glycerin-water mixture was fed from a reservoir through the test section and into a collection bucket. The bucket was weighed to determine the mass flow rate for each test. The mixture was then pumped back to the reservoir and allowed to settle for several hours before the next test. The dye consisted of food coloring mixed with the glycerin-water solution. It was fed from a dye reservoir, through a 0.041 inch diameter tube, into the flow stream. The height of the dye reservoir was adjusted so that the dye would just overcome friction and flow out of the tube very slightly when the glycerin-water mixture was not flowing.

The test section was constructed of aluminum with plexiglas front and back sides. The test plate is illustrated in Figure 13. It was made of one inch thick plexiglas, with seven 1.3283 inch diameter holes drilled through it, four inches apart, in a hexagonal pattern. The hole diameter was chosen so that the porosity of the center hole, given by its area divided by the hexagonal area associated with it, was equal to 10%. The hexagonal pattern of holes meant that the center hole was actually being fed from a hexagonal cross section upstream of the hole. The theoretical solution assumed a circular cross section upstream. This difference is illustrated in Figure 14.

---

[1] This is discussed again later in this section.

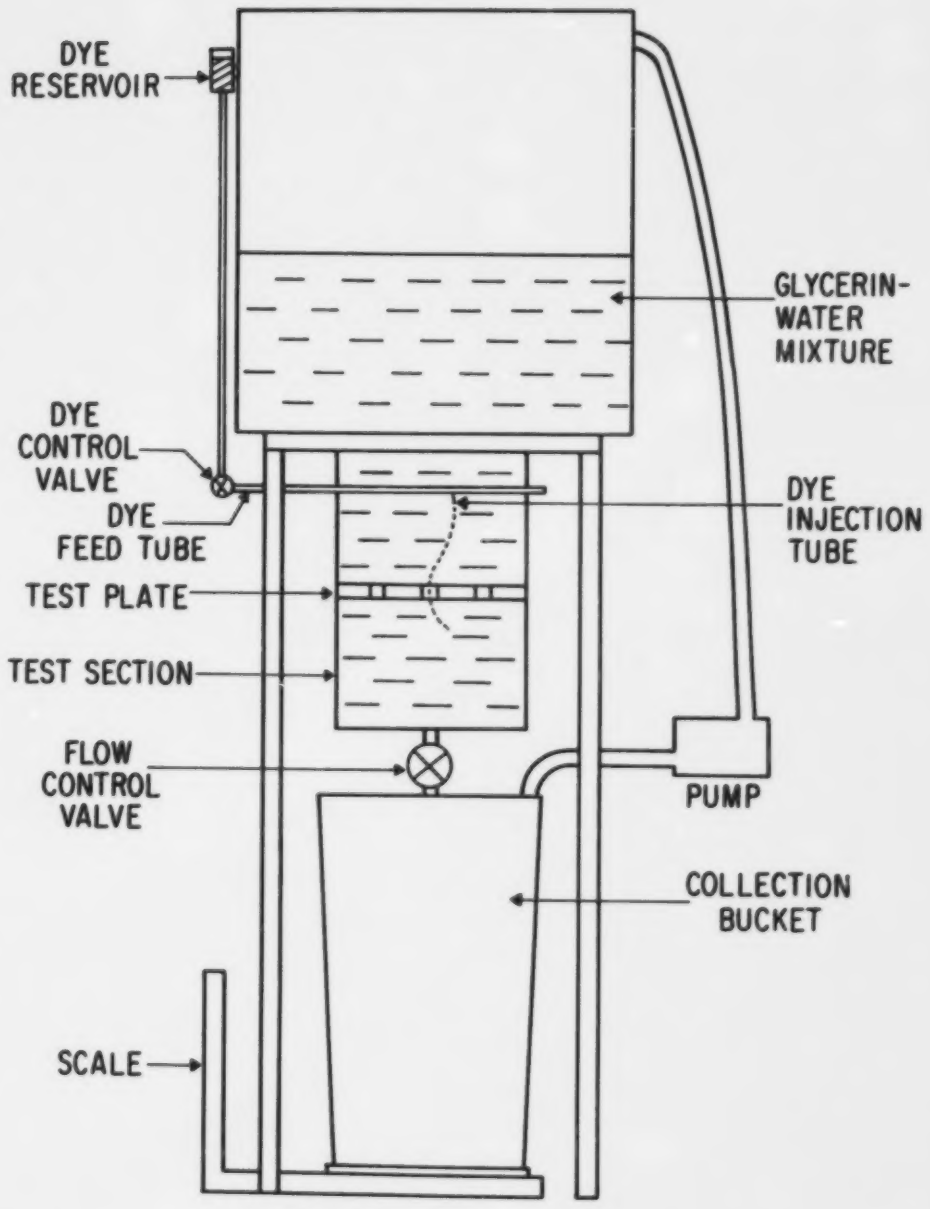

Figure 12. Apparatus for the flow visualization experiment.

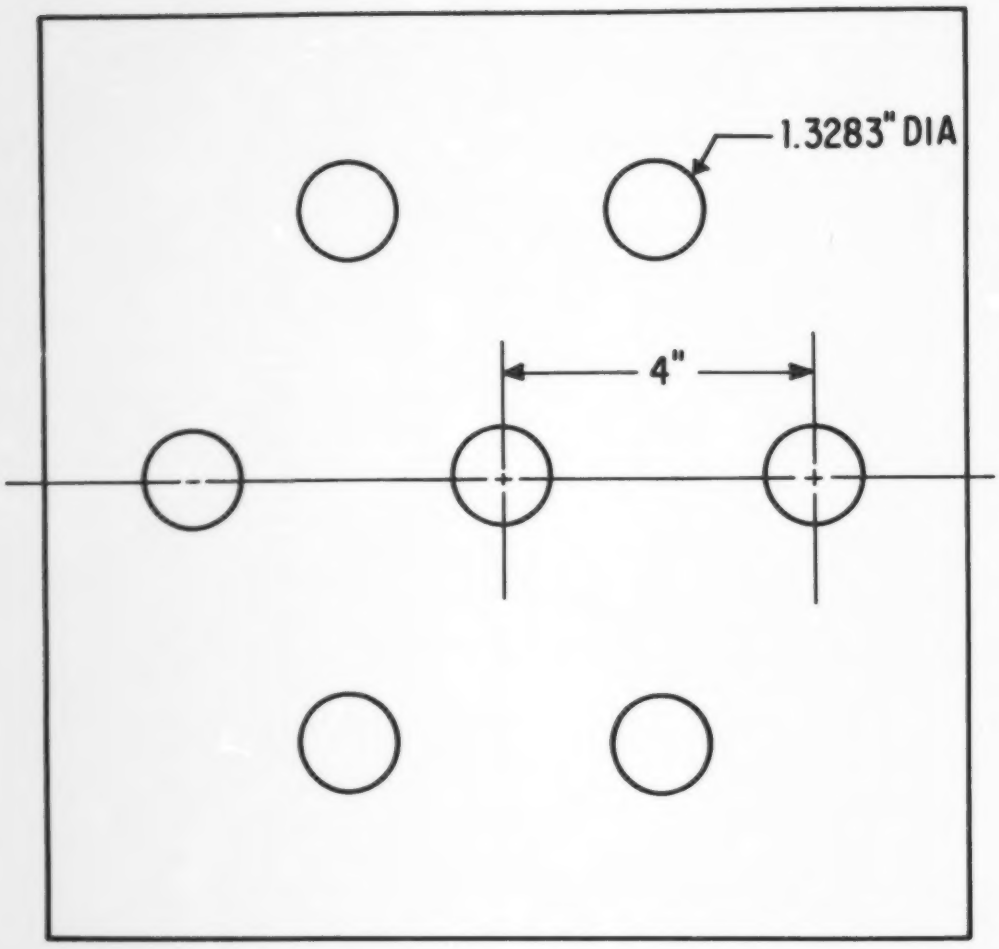

Figure 13. Plexiglas test plate for the flow visualization experiment.

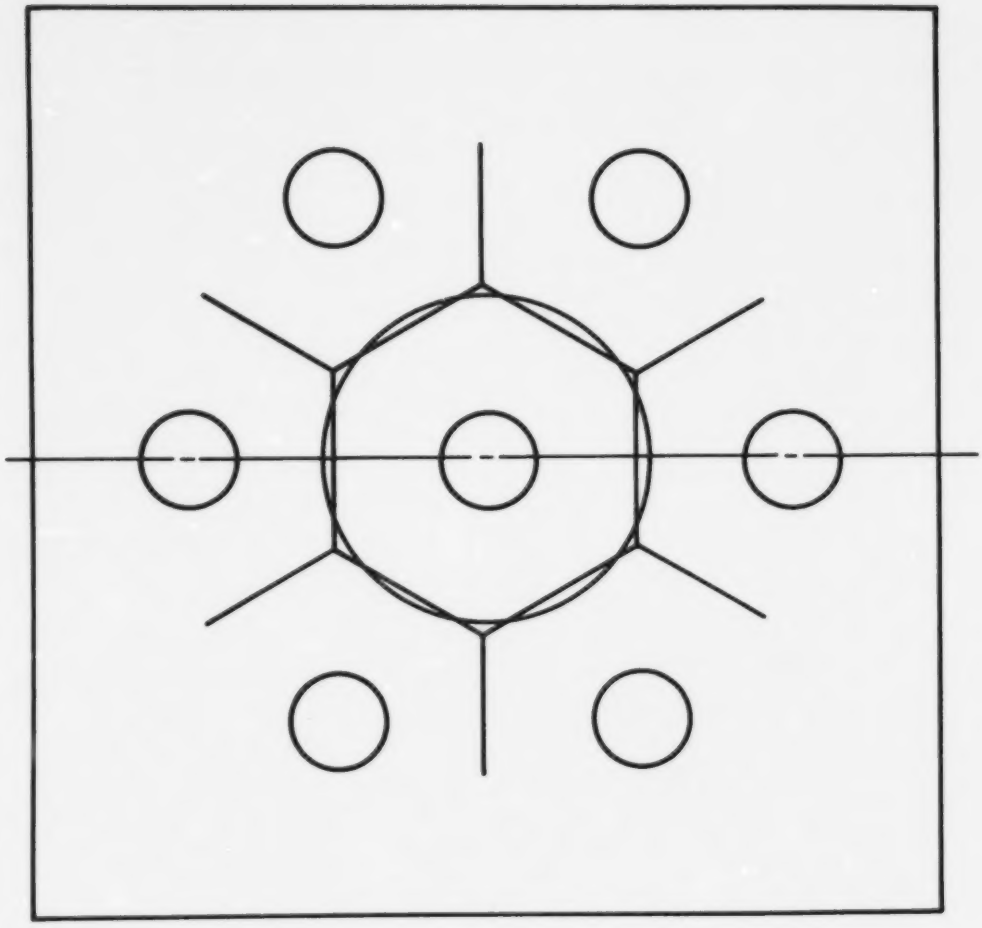

Figure 14. Test plate with the boundaries imposed upon the theoretical and physical pore models.

BEGIN FIRST LINE OF TEXT HERE
TYPING GUIDE SHEET
CENTER OF PAGE
TOP OF IMAGE AREA
DROPPED HEAD: BEGIN SECTIONS HERE

Dye was injected in the plane of the centerlines shown in Figure 13. The dye injection tube was very delicate and could not be adjusted exactly perpendicular to the plate without a more elaborate experimental setup, including a fine adjustment for the dye injection tube. Thus the streamlines actually started with some velocity perpendicular to the plane of the desired streamline. For Re = 5 and 8, this effect seemed to damp itself out. However a smooth, two-dimensional streamline for Re = 2, could not be obtained with the present experimental setup.

Control of the Experimental Reynolds Number

To obtain a sufficiently low Reynolds number, it was necessary to adjust the fluid viscosity. The hole diameter was fixed in size and had to be large enough to allow the streamlines to be photographed and measured easily. The flow rate could only be adjusted within limits. Too large a flow rate caused the pressure head to decrease too rapidly and thus weakened the assumption of quasi-steady flow. Too slow a flow rate was thought to exaggerate the disturbing influences on the streamlines; such as the influences of the test section wall, and of the dye injection tube, on the flow pattern. It was found that the present experimental setup could not maintain a smooth, two-dimensional streamline with a flow rate below about 1/4 ft^3/min. Therefore, to keep Re < 10, the kinematic viscosity had to be very large. It was found that a mixture of about 87% by volume of glycerin, and 13% by volume water gave a satisfactory kinematic viscosity. The viscosity of glycerin is very sensitive to temperature. Figure 15 shows the experimental temperature versus kinematic viscosity curve for the mixture used in this experiment. This curve was obtained by using a Saybolt viscometer, and allowing the solution temperature to vary with the day to day room temperature. Daily variations in the temperature, and hence the viscosity, caused the Reynolds number to vary for each test. The average Reynolds number has been used in determining theoretical streamlines for comparison to the experimental streamlines. The actual Reynolds numbers for each test are given in TABLES 1 and 2.

Results

The experimental streamlines were photographed, and were measured and transferred by hand, as data points, onto the theoretical curves. The results are presented for average Reynolds numbers of 5 and 8, in Figures 16 and 17. The experimental streamlines fit well with the families of theoretical streamlines. Some error at the larger radial distances may be due to the difference between the physical and theoretical upstream flow cross sections. Also the fluctuation of Reynolds number with temperature has probably caused some inaccuracy.

The purpose of this experiment was to gain confidence in the theoretical flow field solution. No attempt was made to directly model the actual filter or the deposition of particles from the flow. The experiment was designed to model, as closely as possible, the assumptions and boundary conditions of the theoretical flow field model. To this extent, the results have been

BEGIN LAST LINE OF TEXT HERE
BOTTOM OF IMAGE AREA, OUTSIDE DIMENSION FOR TABLES AND ILLUSTRATIONS
3/8"

PAGE NUMBER
EPA-267 (Cin.)
(4-76)

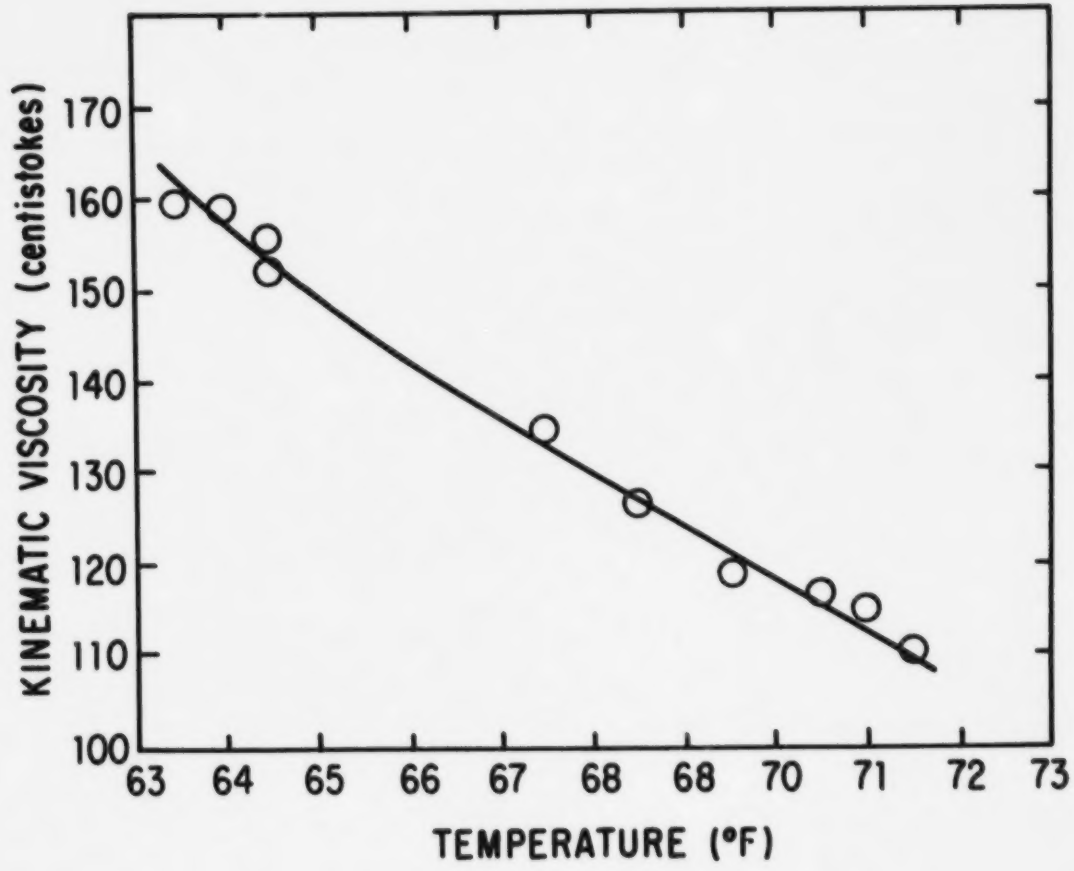

Figure 15. Experimental temperature-viscosity curve for the glycerin-water mixture (about 87% by volume glycerin).

BEGIN FIRST LINE OF TEXT HERE
TYPING GUIDE SHEET
CENTER OF PAGE
TOP OF IMAGE AREA
DROPPED HEAD BEGIN SECTIONS HERE

TABLE 1. ACTUAL REYNOLDS NUMBERS FOR THE FLOW VISUALIZATION EXPERIMENT

Average Reynolds number = 5

Temperature (F)	Kinematic Viscosity (cs)	Flow Rate (cfm)	Experimental Reynolds Number
69.0	123	0.280	6
68.8	124	0.283	6
67.0	136	0.276	5
66.8	137	0.275	5
67.0	136	0.273	5
68.6	127	0.278	5 1/2
64.0	160	0.247	4

TABLE 2. ACTUAL REYNOLDS NUMBERS FOR THE FLOW VISUALIZATION EXPERIMENT

Average Reynolds number = 8

Temperature (F)	Kinematic Viscosity (cs)	Flow Rate (cfm)	Experimental Reynolds Number
68.3	128	0.468	9 1/2
67.6	134	0.454	8 1/2
65.9	144	0.448	8
66.1	142	0.448	8
63.0	166	0.435	7
64.5	156	0.439	7
64.0	160	0.435	7
65.2	149	0.444	7 1/2

BEGIN LAST LINE OF TEXT
BOTTOM OF IMAGE AREA, OUTSIDE DIMENSION FOR TABLES AND ILLUSTRATIONS
3/8"

PAGE NUMBER
EPA-287 (Cle.)
(4-76)

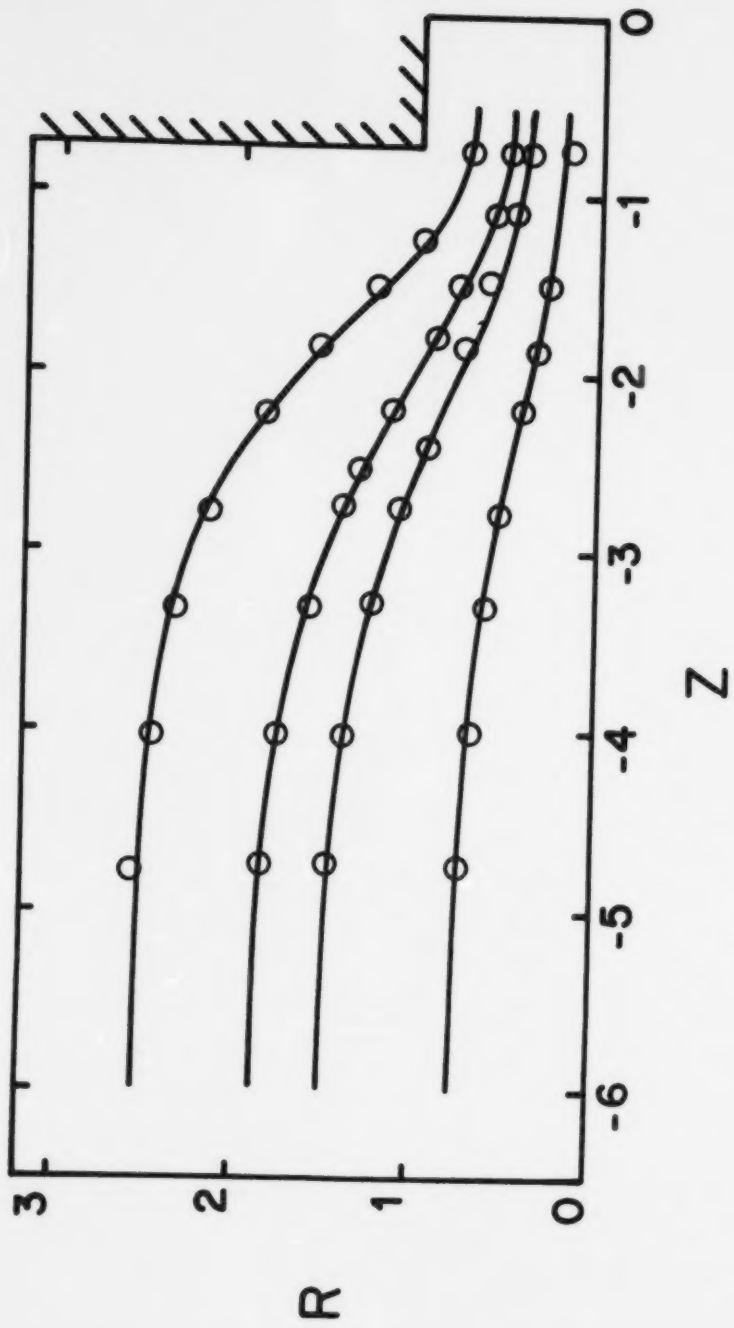

Figure 16. Experimental streamlines (data points) compared to the theoretical streamlines Re = 5, P = 10%, T = 0.75 D_{pore}.

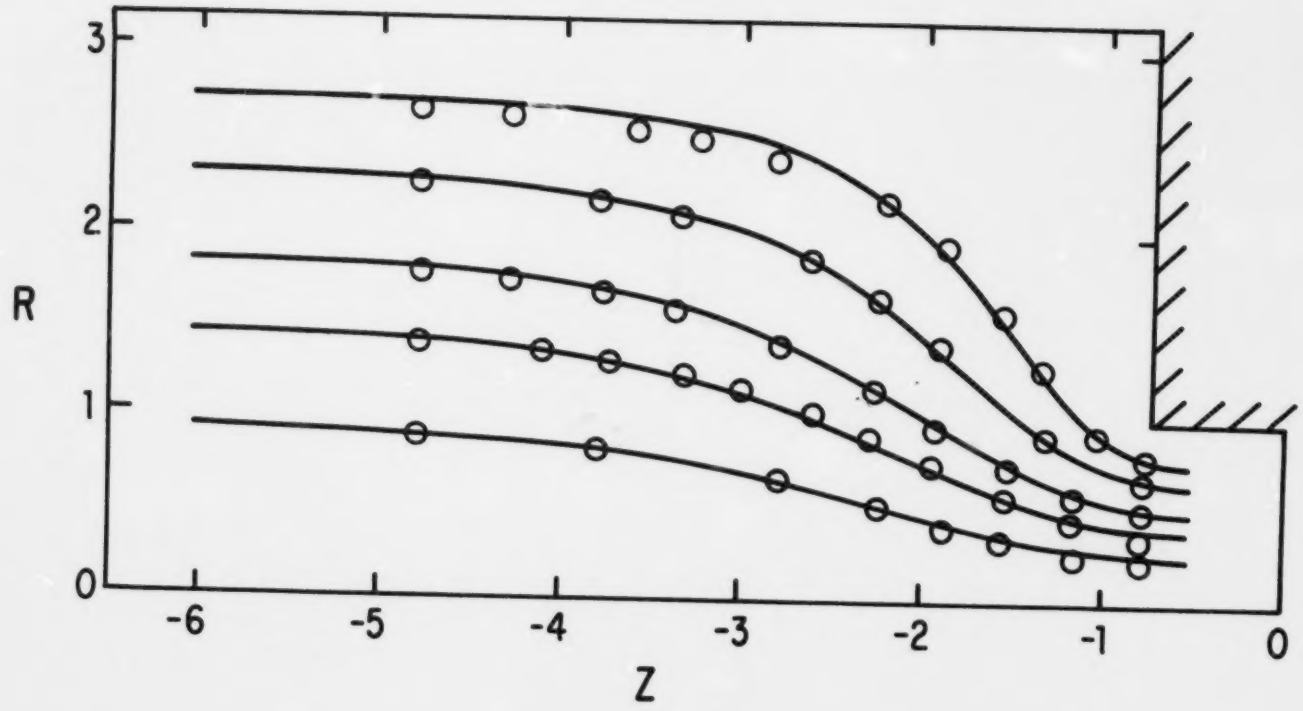

Figure 17. Experimental streamlines (data points) compared to the theoretical streamlines Re = 8, P = 10%, T = 0.75 D_{pore}.

BEGIN FIRST LINE OF TEXT HERE
TYPING GUIDE SHEET
CENTER OF PAGE
TOP OF IMAGE AREA
DROPPED HEAD: BEGIN SECTIONS HERE
6-1/2"
9-1/8"
BEGIN LAST LINE OF TEXT
BOTTOM OF IMAGE AREA; OUTSIDE DIMENSION FOR TABLES AND ILLUSTRATIONS
3/8"
PAGE NUMBER
EPA-287 (Cin.)
(4-76)

satisfactory. In the remainder of this work, therefore, the flow field generated by the computer solution to the Navier-Stokes equations has been considered to be accurate.

BEGIN FIRST LINE OF TEXT HERE
TYPING GUIDE SHEET
CENTER OF PAGE
TOP OF IMAGE AREA
DROPPED HEAD. BEGIN SECTIONS HERE

SECTION 4

PARTICLE TRAJECTORIES AND FILTER IMPACTION EFFICIENCIES

INTRODUCTION

The primary objective of this study has been to develop a procedure for predicting theoretical impaction efficiencies for a large pore Nuclepore filter. The solution to the Navier-Stokes equations, presented and discussed in SECTION 3, expressed the flow field through the filter pore in terms of stream function values at finite difference grid points. With this information, it was possible to predict the trajectory of a particle suspended in, and moving with the flow stream. The inertia of the particle would cause it to separate from its initial streamline, to move across the converging flow pattern, and to deposit on the filter surface as the airstream bent around, and passed through the pore. It has been assumed that all particles adhere to the filter surface upon impact. This assumption may be inaccurate, but it was considered a necessary first approximation.

Particle trajectories were obtained following a similar procedure to that used by Marple and Liu (18) in their study of jet impactors. The first problem was to determine the velocity field from the stream function solution. Stokes' drag forces were then applied to obtain the equations motion for the particle, which were solved to determine the particle trajectory. It was possible to determine a critical trajectory for impaction, and from this, a theoretical impaction efficiency. By considering the particle to impact whenever its center of mass passed within one particle radius of the filter, the interception and inertial impaction effects were incorporated into a single impaction efficiency.

CALCULATION OF THE VELOCITY FIELDS

The solution to the Navier-Stokes equations gave the values of the stream function at each grid point. Before this information could be used to determine particle trajectories, it was necessary to express the flow field in terms of the axial and radial velocity fields. The axial and radial velocities are related to the stream function through equations (3-13) and (3-14).

$$U = -\frac{1}{R}\frac{\partial \psi}{\partial R} \qquad (3\text{-}13)$$

BOTTOM OF IMAGE AREA OUTSIDE DIMENSION FOR TABLES AND ILLUSTRATIONS
BEGIN LAST LINE OF TEXT
3/8"

PAGE NUMBER
EPA-287 (Cln.) (4-76)

BEGIN FIRST LINE OF TEXT HERE
TYPING GUIDE SHEET
CENTER OF PAGE
TOP OF IMAGE AREA
DROPPED HEAD; BEGIN SECTIONS HERE

$$V = + \frac{1}{R} \frac{\partial \psi}{\partial Z} \qquad (3\text{-}14)$$

The values of U and V at every interior grid point were obtained from central difference approximations to the first derivatives of ψ. At the pore entrance and exit, and at the last radial grid line before the hypothetical tube boundary, the appropriate variable mesh difference equations were used. These special cases were discussed in SECTION 3. The non-dimensional velocity at $Z = \pm \infty$, is equal to the area ratio $\left(\frac{\pi R_1^2}{\pi R_2^2}\right)$, and thus is equal to the filter porosity. The non-slip condition imposes zero velocities on the filter surfaces. The axial velocity along the pore centerline was approximated by the forward difference formula

$$U_{1,j} = \frac{1}{3} (4U_{2,j} - U_{3,j}) \qquad (4\text{-}1)$$

Here j represents any axial grid line (column), and the subscripts 1, 2, and 3 indicate the centerline or the first, second, and third radial grid lines (rows). This formula, derived in Appendix A, was obtained from a Taylor series expansion, noting that $\frac{\partial U}{\partial R} = 0$ on the pore centerline. The axial velocity along the hypothetical tube boundary was obtained in a similar manner. However the formula was more complicated because the radial grid spacing is not uniform around the last but one radial grid line. The Taylor series expansion for this case gives

$$U_{NPT,j} = \frac{\frac{dn}{h_R(h_R + dn)} U_{NPT-2,j} - \frac{h_R + dn}{h_R\, dn} U_{NPT-1,j}}{\frac{dn}{h_R(h_R + dn)} - \frac{h_R + dn}{h_R\, dn}} \qquad (4\text{-}2)$$

Here NPT denotes the hypothetical tube boundary, and NPT-1, NPT-2 denote the first and second radial grid lines below NPT. This formula is derived in Appendix A.

THEORY FOR PARTICLE TRAJECTORIES

The particle trajectory calculations were based upon the assumption that the fluid force on the particle could be predicted by Stokes' equation for the viscous drag on a sphere[1].

---

[1] Stokes' equation has been taken from Schlichting (15), p. 106.

BEGIN LAST LINE OF TEXT HERE
BOTTOM OF IMAGE AREA, OUTSIDE DIMENSION FOR TABLES AND ILLUSTRATIONS
3/8"

PAGE NUMBER
EPA-287 (Cin.1 (4-76)

$$DRAG = 3\pi\mu_f d_p(\bar{V}_f - \bar{V}_p) \qquad (4\text{-}3)$$

The equations of motion of a particle were obtained by applying Newton's second law of motion to a particle undergoing Stokes' drag forces. The equations of motion, non-dimensionalized with respect to R_1 and U_1, are presented as equations (4-4) and (4-5). The non-dimensional position of the particle is defined by R and Z.

$$\xi \frac{d^2R}{dt^2} = V(R,Z) - \frac{dR}{dt} \qquad (4\text{-}4)$$

$$\xi \frac{d^2Z}{dt^2} = U(R,Z) - \frac{dZ}{dt} \qquad (4\text{-}5)$$

The dimensionless inertial parameter, ξ, occurs as

$$\xi = \frac{\rho_p U_1 d_p^2}{18\mu_f R_1} \qquad (4\text{-}6)$$

The Knudsen number for a 1μm particle is not greatly less than unity (see SECTION 3). Therefore the inertial parameter, ξ, has been multiplied by the Cunningham correction for slip, C, as presented by Stern, et al. (10).

$$C = 1 + \frac{2\lambda}{d_p}\left(1.23 + 0.41 \exp(-0.44\, d_p/\lambda)\right) \qquad (4\text{-}7)$$

The inertial parameter becomes

$$\xi = \frac{C\rho_p U_1 d_p^2}{18\mu_f R_1} \qquad (4\text{-}8)$$

Introduction of the Reynolds number from SECTION 3.

$$Re = \frac{2 R_1 U_1 \rho_f}{\mu_f} \qquad (3\text{-}12)$$

enables the inertial parameter to be written in the form

$$\xi = C \frac{Re}{9} \frac{\rho_p}{\rho_f} \left(\frac{d_p}{2R_1}\right)^2 \qquad (4\text{-}9)$$

In this form it may be seen that ξ is a function of the Cunningham slip correction factor (related to the ratio of the particle diameter to the mean free path of the air molecules), the characteristic Reynolds number (the ratio of inertial fluid forces to the viscous fluid forces), the particle to fluid density ratio, and the ratio of the particle diameter to the pore diameter. The parameter, ξ, is often termed the Stokes number. Particles with the same value of ξ will follow similar center of mass trajectories in similar flow fields.

Equations (4-4) and (4-5) are second order ordinary differential equations. Before solving them, it is convenient to write them as four first order equations.

$$\frac{dR}{dt} = V_p \qquad (4\text{-}10)$$

$$\frac{dZ}{dt} = U_p \qquad (4\text{-}11)$$

$$\frac{dV_p}{dt} = \frac{1}{\xi}\left(V(R,Z) - V_p\right) \qquad (4\text{-}12)$$

$$\frac{dU_p}{dt} = \frac{1}{\xi}\left(U(R,Z) - U_p\right) \qquad (4\text{-}13)$$

Equations (4-10), (4-11), (4-12), and (4-13) were solved by a fourth order Runge-Kutta method, to obtain the particle trajectory in terms of the particle position (R,Z) and velocity at each step of the Runge-Kutta integration. It was necessary to specify initial conditions for the integration. The particle was given an initial position far upstream, and an initial velocity equal to the fluid velocity. the upstream coordinate transformation

$$\eta_u = \tanh\left(k_u(Z + Z_o)\right) \qquad (3\text{-}18)$$

made it necessary to change equation (4-11), when in the upstream region, to

$$\frac{d\eta_u}{dt} = k_u U_p (1 - \eta_u^2) \qquad (4\text{-}11a)$$

Equations (4-10), (4-12), and (4-13) remained unchanged in the upstream region. V and U are the radial and axial fluid velocities at the particle position (R,η_u) upstream of the pore, and (R,Z) within the pore. Trajectories were not calculated downstream of the pore.

NUMERICAL SOLUTION

The Runge-Kutta routine was taken from Carnahan, et al. (19). The Runge-Kutta method was chosen over the predictor-corrector methods because of the ease with which the Runge-Kutta step size could be controlled during the integration. Carnahan, et al. present a criterion, attributed to Collatz (20), for controlling the step-size in the fourth order Runge-Kutta method used in this work. According to Collatz, if the following criterion is not satisfied, the step size should be decreased.

$$\Delta = \frac{|(k_3 - k_2)|}{|(k_2 - k_1)|} < \varepsilon \qquad (4\text{-}14)$$

The parameters k_1, k_2, and k_3 are the approximate derivative values computed on the interval $x_i \leq x \leq x_{i+1}$.[1] For a step size, h, and a differential equation

$$\frac{dy}{dx} = f(x,y),$$

the parameters k_1, k_2, and k_3 are given as

$$k_1 = f(x_i, y_i)$$

$$k_2 = f\left(x_i + \frac{h}{2},\ y_i + \frac{1}{2} hk_1\right) \qquad (4\text{-}15)$$

$$k_3 = f\left(x_i + \frac{h}{2},\ y_i + \frac{1}{2} hk_2\right)$$

Equation (4-13), for the radial velocity of the particle, was found to be the most critical equation for controlling the step size. If the values of V_p at each step were changing smoothly, it was found that the values of R, Z, and U_p were also changing smoothly. As the step size was increased, it was found that stability problems occurred first with the value of V_p. Therefore k_1, k_2, and k_3 were calculated for equation (4-12), from equations (4-15), and the step size was adjusted accordingly. Collatz suggests that ε be of the order of a few hundredths. A value of $\varepsilon = 0.1$

---

[1] See Carnahan, et al. (19), p. 363.

was sufficient for the present solutions. The value of Δ was checked at each integration step, and if it became greater than 0.1, the step size was halved.

The step by step procedure for obtaining particle trajectories is summarized below:

1. A particle was started far upstream of the filter, with a velocity equal to the fluid velocity. The initial step size was set at 1/10th the estimated time required for the particle to cross one grid.

2. The fluid velocity at the particle position was obtained by performing a linear interpolation between the fluid velocities at the four surrounding grid points.

3. The equations of motion were integrated with the Runge-Kutta routine to determine a new particle position and velocity. At each integration step, size was checked by equation (4-14), and halved when necessary.

4. The new position was tested to determine whether the particle had crossed a grid line. If it had, the coordinates locating the grid containing the particle were updated. The particle position and velocity were printed after every IPRINT steps.

5. The procedure (steps 2, 3, and 4) was repeated and the particle trajectory was tracked until it either exited the filter pore, impacted on the filter surface, or the maximum allowable integration time, or maximum allowable number of integration steps had been exceeded.

Typical trajectories are shown in Figures 18 and 19. Figure 18 shows the effect of inertia on the particle trajectory. Four different size particles were started at the same upstream position and were followed until they had either impacted or exited the pore. The dashed line represents the streamline initially followed by the particles, and is equivalent to a trajectory for a particle with zero inertia. Figure 19 shows trajectories of particles with the same amount of inertia, but starting from different radial positions. In Figure 19 it can be seen that a critical trajectory would have an initial radial position slightly larger than R = 2.

IMPACTION EFFICIENCIES

The criterion used to determine whether or not a particle has impacted is illustrated in Figure 20. It is presented in the (R,Z) coordinate system for simplicity, however the computer program translates this criterion into the (R,η_u) coordinate system. When the center of mass of a particle has crossed the dashed line in Figure 20, it has either entered the pore or impacted. If it has crossed the dashed line, and its present radial position is above point A, it is considered to have impacted. It was found that any particle entering the pore also exits the pore. Therefore any particle which has crossed the dashed line of Figure 20, and whose radial position is below point A, is considered to have passed through the filter.

BEGIN FIRST LINE OF TEXT HERE
TYPING GUIDE SHEET
CENTER OF PAGE
TOP OF IMAGE AREA
DROPPED HEAD: BEGIN SECTIONS HERE

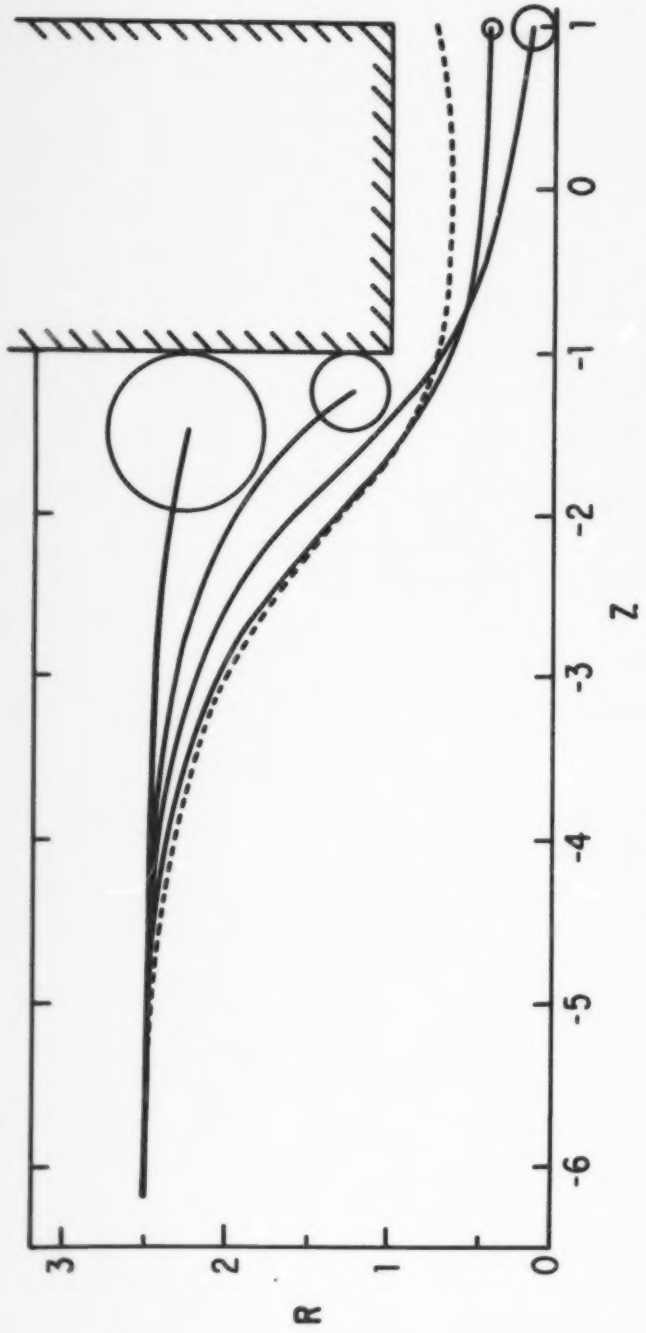

Figure 18. Theoretical particle trajectories for different diameter particles.

BEGIN LAST LINE OF TEXT
BOTTOM OF IMAGE AREA, OUTSIDE DIMENSION FOR TABLES AND ILLUSTRATIONS
3/8"

EPA-287 (Cin.)
(4-76)

BEGIN FIRST LINE OF TEXT HERE
TYPING GUIDE SHEET
CENTER OF PAGE
TOP OF IMAGE AREA
DROPPED HEAD; BEGIN SECTIONS HERE

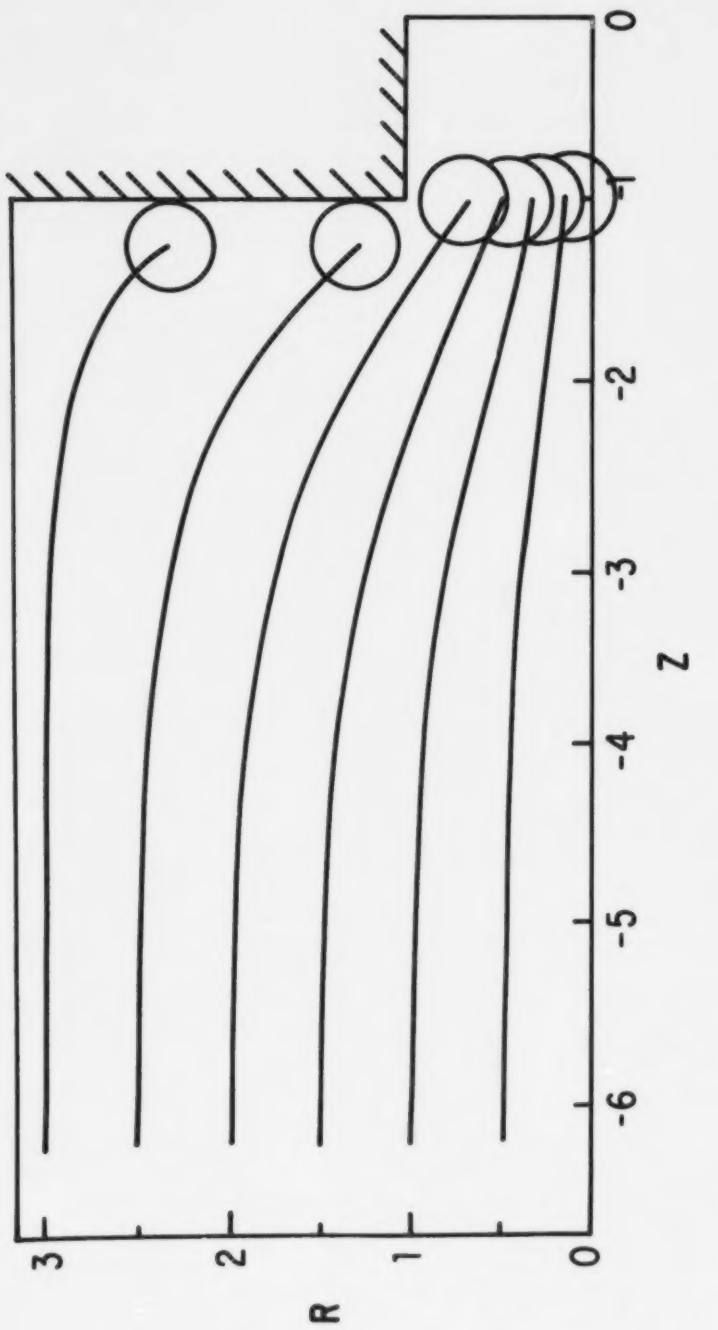

Figure 19. Theoretical particle trajectories for different upstream radial starting positions.

BEGIN LAST LINE OF TEXT
3/8"
BOTTOM OF IMAGE AREA; OUTSIDE DIMENSION FOR TABLES AND ILLUSTRATIONS

EPA-287 (Cin.)
(4-76)

BEGIN FIRST LINE OF TEXT HERE
TYPING GUIDE SHEET
TOP OF IMAGE AREA
DROPPED HEAD; BEGIN SECTIONS HERE

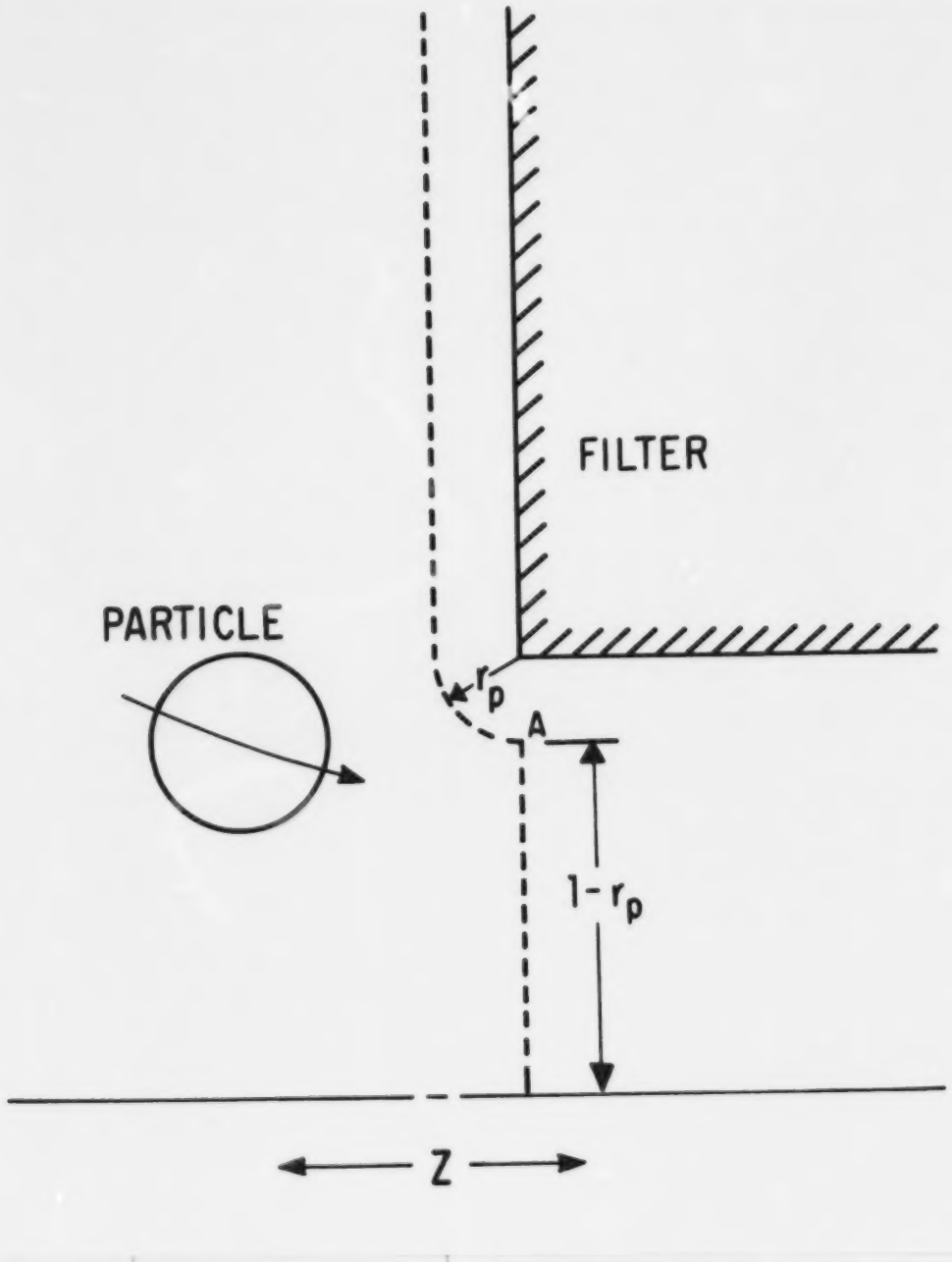

Figure 20. The criterion used to determine particle impaction. To the right of the dashed line, and above point A, impaction occurs.

BEGIN LAST LINE OF TEXT
BOTTOM OF IMAGE AREA; OUTSIDE DIMENSION FOR TABLES AND ILLUSTRATIONS
3/8"

EPA-287 (Cin.)
(4-76)

From Figure 19, it can be inferred that there is a critical trajectory, starting at an upstream critical radius, R_{crit}, such that all particles starting at $R > R_{crit}$ are impacted upon the filter, and all particles starting with $R < R_{crit}$ pass through the filter. The critical trajectory was determined by keeping track of R_{high}, the smallest starting radial position from which the particle still impacted; and keeping track of R_{low}, the largest starting radial position from which the particle still entered the pore. After each trajectory, the new starting position was set at $R = (R_{high} + R_{low})/2$. When the quantity $(R_{high} - R_{low})$ became less than 0.005, the new value of R was considered to have converged to R_{crit}.

The impaction efficiency, E, is related to R_{crit} through the expression

$$E = 1 - \left(\frac{R_{crit}}{\beta}\right)^2 \qquad (4\text{-}16)$$

Here the assumptions of uniform particle concentration and velocity far upstream of the filter have been made. It should be noted that R_{crit} and β are non-dimensionalized with respect to the pore radius. The convergence criterion of 0.005 for the critical radius, gives the impaction efficiency to ± 0.1%.

The computer program used to determine particle trajectories and filter impaction efficiencies for a given flow field, is presented and discussed in detail by Parker (17).

RESULTS AND DISCUSSION

A typical impaction efficiency curve is shown by the solid line in Figure 21. The curve is presented as impaction efficiency versus the non-dimensionalized particle diameter. The impaction efficiency is also a function of Reynolds number, filter thickness, filter porosity, and particle density. It is common practice to present collection efficiency curves in terms of the aerodynamic particle size, defined as $d_p\sqrt{\rho_p}$. The aerodynamic size is an adequate representation of the impaction characteristics of a spherical particle when the characteristic dimensions of the flow field are much greater than the particle diameter. This is equivalent to saying that the interception effect is very small. When interception is relatively important, and the particle diameter is not much smaller than the pore diameter, the collection of particles is a function of both the particle diameter and the aerodynamic size. They must be considered independently.

The broken lines in Figure 21, are impaction efficiency curves for cruder grid spacings in the finite difference network. Therefore Figure 21 indicates how the convergence of the stream function field, as the grid spacing approaches zero, affects the final solution for the impaction efficiency. Figure 22 is an estimate of the effect of further grid refinement. The solid line in Figure 21 was calculated with a grid network which may be represented by h_o. Figure 22 indicates that if the grid spacing were decreased to $h_o/2$, the efficiency at the low end of the curve in

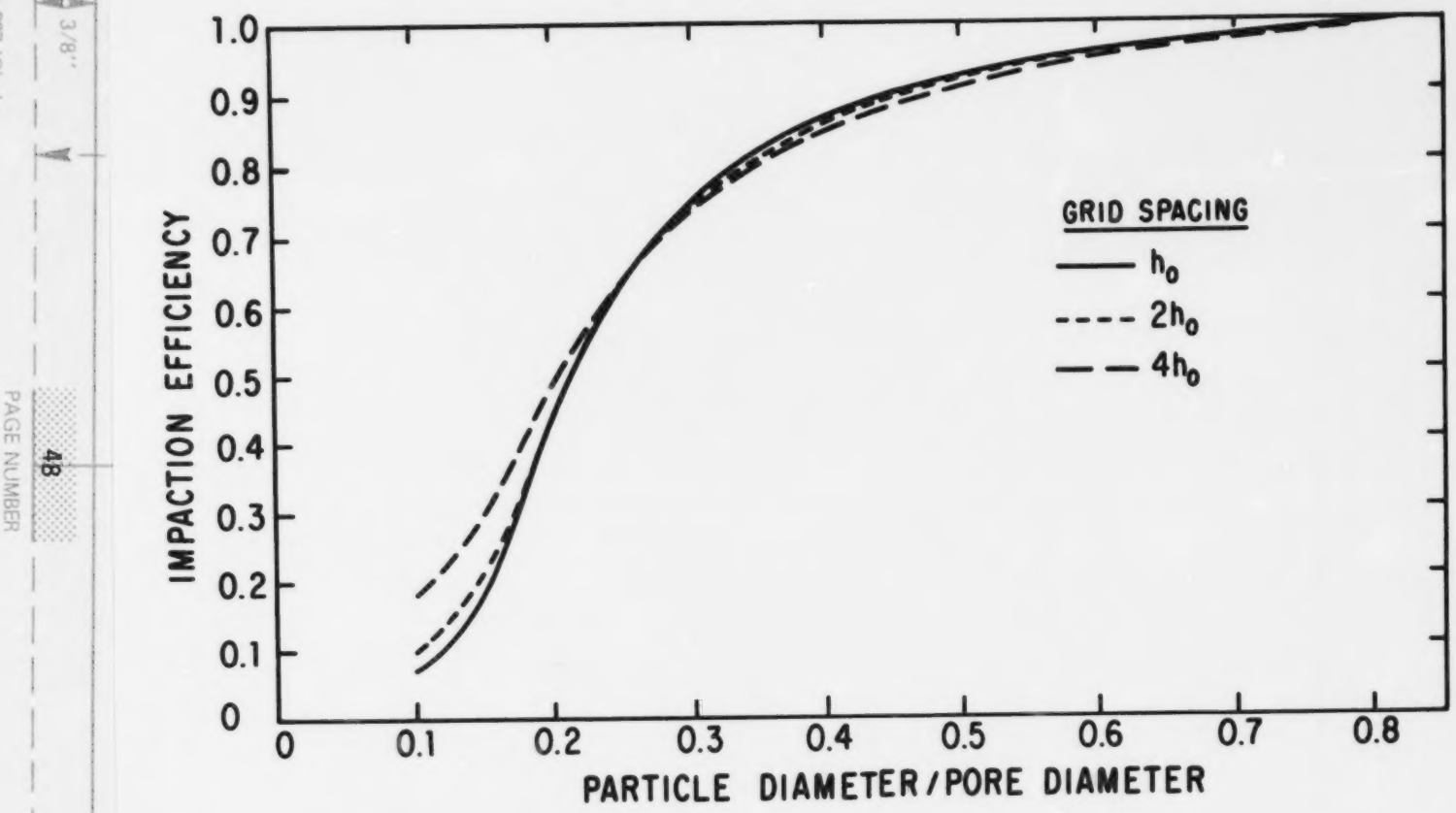

Figure 21. Convergence of the impaction efficiency as the finite difference grid spacing decreases. Re = 2, P = 10%, T = D_{pore}.

BEGIN LAST LINE OF TEXT
DROPPED HEAD; BEGIN SECTIONS HERE
BEGIN FIRST LINE OF TEXT HERE
TYPING GUIDE SHEET
EPA-287 (Cin.) (4-76)
3/8"
PAGE NUMBER
48
CENTER OF PAGE
BOTTOM OF IMAGE AREA; OUTSIDE DIMENSION FOR TABLES AND ILLUSTRATIONS
TOP OF IMAGE AREA

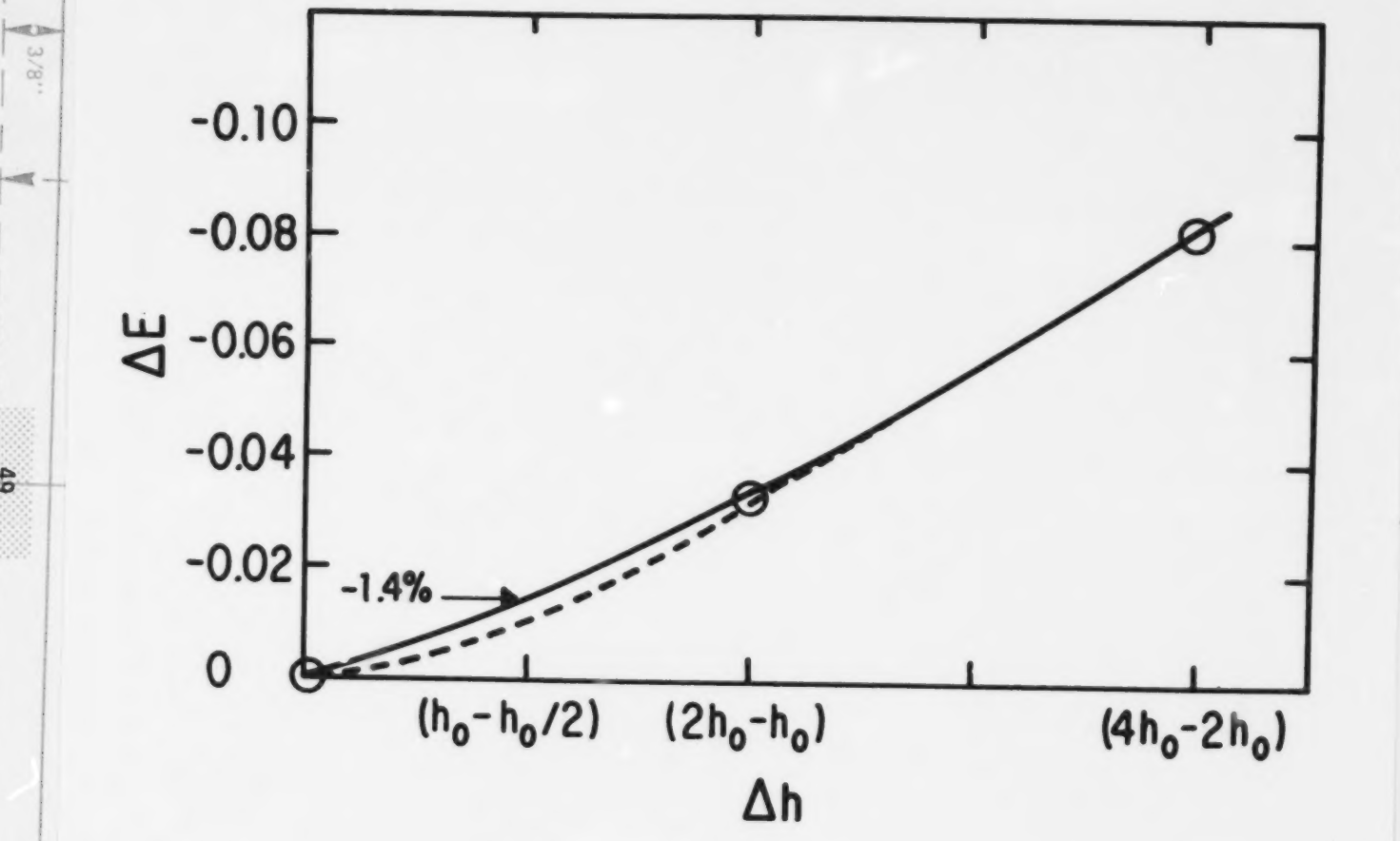

Figure 22. Estimate of the effect of further grid refinement on the impaction efficiency curve. ΔE represents the change in impaction efficiency corresponding to a change in the grid spacing of Δh.

TYPING GUIDE SHEET
BEGIN FIRST LINE OF TEXT HERE
CENTER OF PAGE
TOP OF IMAGE AREA
BOTTOM OF IMAGE AREA, OUTSIDE DIMENSION FOR TABLES AND ILLUSTRATIONS
3/8"
PAGE NUMBER
49
EPA-287 (Cin.) (4-76)

Figure 21 would decrease by 1.4% or less. The dashed line in Figure 22 was obtained by assuming that the curve comes in to the origin smoothly. If this were the case, the decrease in efficiency would be less than 1%. In either case, the impaction efficiency curve has converged to better than 1.5%.

The grid space, h_o, represents the finest grid network considered. The actual grid spacing varied for each region of the solution (upstream, pore, and downstream). Also the last radial grid was a different size than the other radial grids, in order to accomodate a variable porosity. The grid network corresponding to h_o consisted of : 48 upstream axial grids, 24 axial grids inside the pore, 24 downstream axial grids, 12 radial grids inside the pore, and 38 radial grids in the upstream and downstream regions.

BEGIN FIRST LINE OF TEXT HERE
TYPING GUIDE SHEET
CENTER OF PAGE
TOP OF IMAGE AREA
DROPPED HEAD: BEGIN SECTIONS HERE

SECTION 5

IMPACTION EFFICIENCY STUDY

INTRODUCTION

The computational procedure developed in SECTIONS 3 and 4 has been applied to study the effects of certain parameters on the impaction efficiency of the filter, and the results are presented. The parameters that have been considered in this study are the pore Reynolds number, the particle density, the filter thickness, and the filter porosity.

THE EFFECT OF PORE REYNOLDS NUMBER

Figure 23 shows the effect of the pore Reynolds number for a fixed particle density, pore diameter, filter thickness, and filter porosity. Reynolds numbers of 1, 2, and 3 were found to span the range of desired cut-points (50% efficiency for particle diameters from 2 to 3.5μm). As the Reynolds number increases, the flow rate and the velocity through the pore increases, and the impaction efficiency increases as a result of the increased inertia of the faster moving particles.

THE EFFECT OF PARTICLE DENSITY

Because the interception of particles is an important deposition mechanism, the particle diameter and particle density are independent parameters. Figures 24, 25, and 26 show the effect of particle density on the impaction efficiency curves, for the three Reynolds numbers considered earlier. The increase in particle density causes an increase in mass for a given diameter particle. The increase in mass corresponds to an increase in particle inertial and thus an increase in the impaction efficiency.

THE EFFECT OF FILTER THICKNESS

The effect of filter thickness is shown in TABLE 3. It appears that the impaction efficiency is slightly increased as the filter thickness increases. This effect is not the result of impaction within the pores, but is the result of the effect of filter thickness on the converging upstream streamlines. The effect is very small and therefore it may be concluded that variations in the filter thickness will not significantly change the filter impaction efficiency.

BEGIN LAST LINE OF TEXT
BOTTOM OF IMAGE AREA OUTSIDE DIMENSION FOR TABLES AND ILLUSTRATIONS
3/8"

PAGE NUMBER
EPA-267 (Cin.)
(4-76)

BEGIN FIRST LINE OF TEXT HERE

TYPING GUIDE SHEET

CENTER OF PAGE

TOP OF IMAGE AREA

DROPPED HEAD; BEGIN SECTION HERE

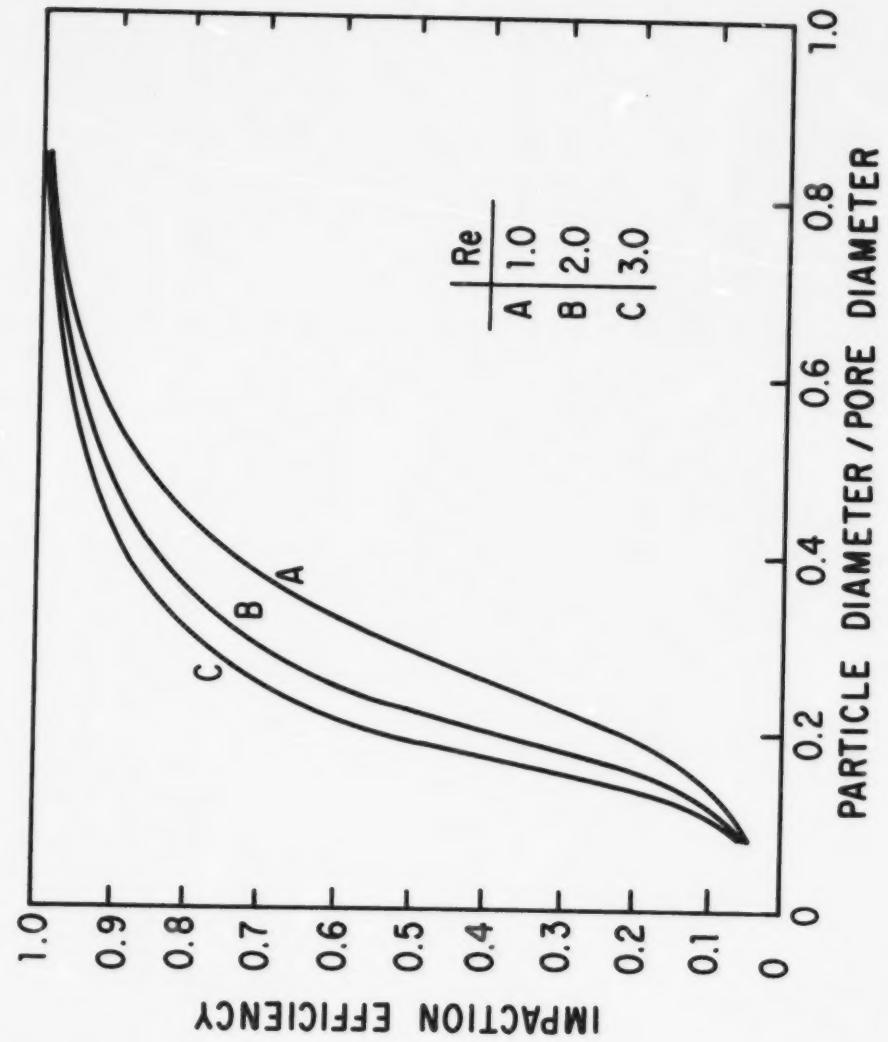

Figure 23. Effect of Reynolds number on the impaction efficiency. P = 10%, T = D_{pore}, ρ_p = 1.0g/cm^3

BEGIN LAST LINE OF TEXT

3/8"

BOTTOM OF IMAGE AREA; OUTSIDE DIMENSION FOR TABLES AND ILLUSTRATIONS

PAGE NUMBER

EPA-287 (Cin.) (4-76)

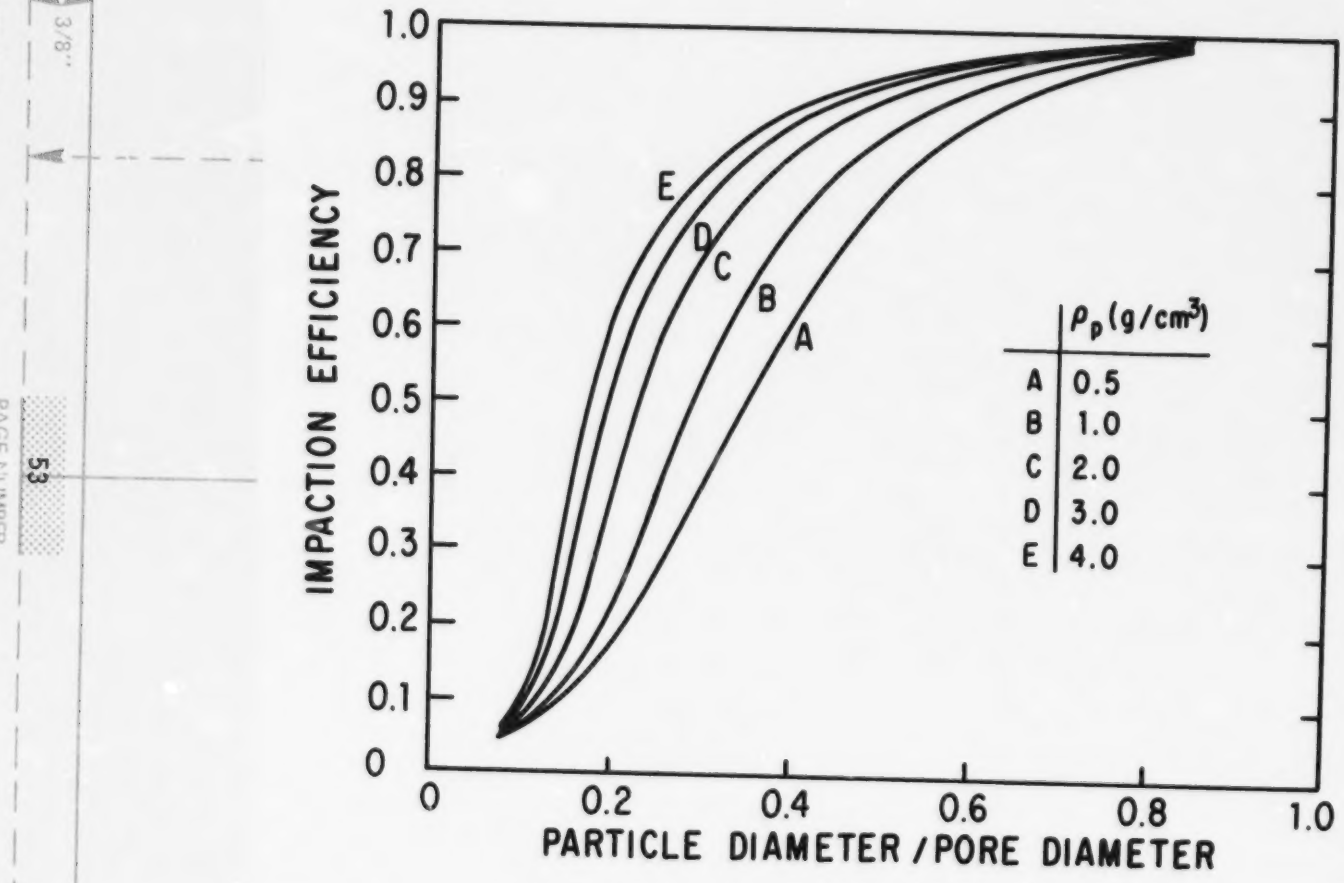

Figure 24. Effect of particle density on the impaction efficiency. Re = 1, P = 10%, T = D_{pore}.

BEGIN LAST LINE OF TEXT
3/8"
EPA-287 (Cin.) (4-76)
PAGE NUMBER
53
BOTTOM OF IMAGE AREA, OUTSIDE DIMENSION FOR TABLES AND ILLUSTRATIONS
DROPPED HEAD: BEGIN SECTION HERE
BEGIN FIRST LINE OF TEXT HERE
TYPING GUIDE SHEET
CENTER OF PAGE
TOP OF IMAGE AREA

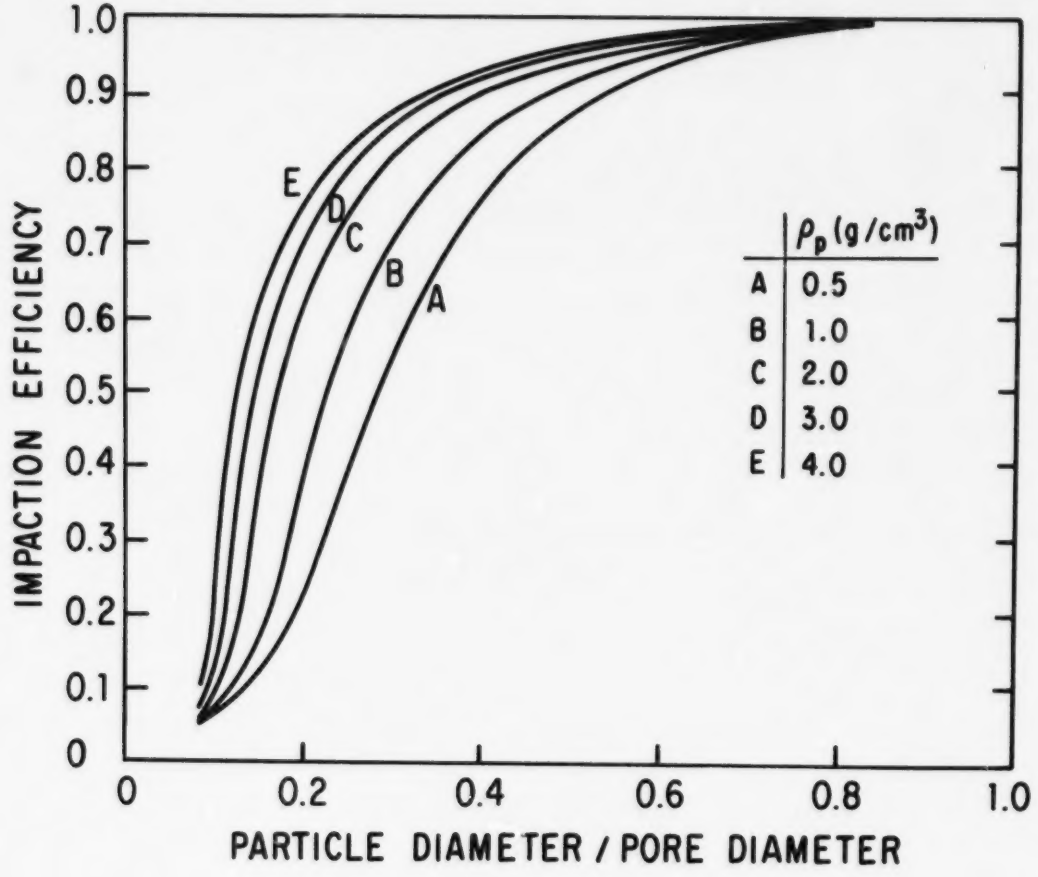

Figure 25. Effect of particle density on the impaction efficiency. Re = 2, P = 10%, T = D_{pore}.

BEGIN LAST LINE OF TEXT
3/8"
EPA-287 (Cim.) (4-76)
PAGE NUMBER
54
BOTTOM OF IMAGE AREA; OUTSIDE DIMENSION FOR TABLES AND ILLUSTRATIONS
BEGIN FIRST LINE OF TEXT HERE
DROPPED HEAD; BEGIN SECTIONS HERE
TYPING GUIDE SHEET
CENTER OF PAGE
TOP OF IMAGE AREA

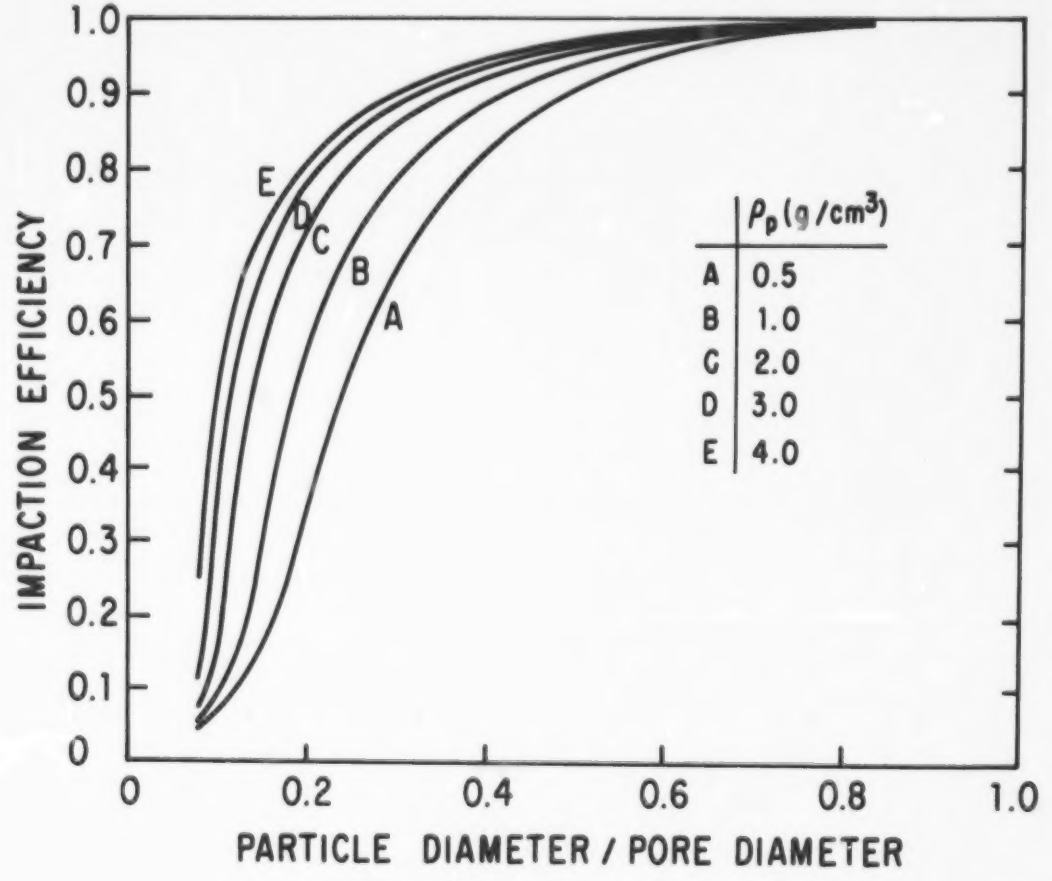

Figure 26. Effect of particle density on the impaction efficiency. Re = 3, P = 10%, T = D_{pore}.

BEGIN LAST LINE OF TEXT
3/8"
EPA-287 (Cin.) (4-76)
PAGE NUMBER
55
BOTTOM OF IMAGE AREA, OUTSIDE DIMENSION FOR TABLES AND ILLUSTRATIONS
DROPPED HEAD, BEGIN SECTION HERE
BEGIN FIRST LINE OF TEXT HERE
TYPING GUIDE SHEET
CENTER OF PAGE
TOP OF IMAGE AREA

TABLE 3. THE EFFECT OF FILTER THICKNESS ON THE IMPACTION EFFICIENCY

Particle Diameter (μm)	Impaction Efficiency T = 10μm	T = 12μm	T = 14μm
1.0	4.6	4.8	5.0
1.2	5.8	6.0	6.2
1.8	11.1	11.5	11.8
2.1	15.3	15.8	16.2
2.4	20.7	21.4	21.9
3.0	36.3	36.9	37.4
3.6	52.3	52.9	53.3
4.2	65.0	65.3	65.7
4.8	74.2	74.5	74.7
5.4	81.0	81.2	81.5
6.0	86.1	86.3	86.4
6.6	89.9	90.0	90.2
7.2	92.8	92.9	93.0
8.4	96.6	96.6	96.7
10.0	99.1	99.2	99.2

THE EFFECT OF FILTER POROSITY

To determine the effect of filter porosity on the efficiency curve, it was decided to consider a constant flow rate (and thus a constant face velocity). The pore Reynolds number is related to the porosity and flow rate through equation (5-8).

$$Re = \frac{D_{pore}}{\nu P} \frac{Q}{A_f} \qquad (5\text{-}8)$$

Therefore, to vary the porosity and hold the flow rate constant, it was necessary to allow the pore Reynolds number to vary. The results are presented in TABLE 4. The impaction efficiency appears to be slightly increasing with increasing porosity, except for large particle diameters where it seems to be constant or to decrease slightly. The convergence criterion for the critical trajectory gave an impaction efficiency that was accurate to within ± 0.1% (see SECTION 4). Therefore the decrease in efficiency

noticeable for the large particles may be an artifact due to fluctuations in the efficiency caused by the convergence criterion. The increasing efficiency with porosity observed for smaller particles, however, is a surprising result. Intuitively, one would expect that the more porous the filter, the less efficient it would be. Thus, as the porosity approached 100%, the efficiency should approach zero. the results presented in TABLE 4 appear to indicate the opposite trend.

TABLE 4. THE EFFECT OF FILTER POROSITY ON THE IMPACTION EFFICIENCY

Particle Diameter (μm)	Impaction Efficiency P = 8%	P = 10%	P = 12%
1.0	0.046	0.048	0.051
1.2	0.057	0.060	0.064
1.8	0.106	0.115	0.124
2.1	0.146	0.158	0.169
2.4	0.195	0.214	0.232
3.0	0.341	0.369	0.392
3.6	0.505	0.529	0.546
4.2	0.640	0.653	0.663
4.8	0.737	0.745	0.750
5.4	0.809	0.812	0.815
6.0	0.861	0.863	0.864
6.6	0.900	0.900	0.901
7.2	0.929	0.929	0.928
8.4	0.967	0.966	0.966
10.0	0.991	0.992	0.991

The method used to increase the filter porosity involved changing the geometry of the stream tube. The stream tube/pore radius ratio, β, was decreased, causing a corresponding increase in porosity according to equation (3-1).

$$P = \frac{1}{\beta^2} \qquad (3\text{-}1)$$

The pore diameter remained unchanged, and therefore the increase in porosity was equivalent to increasing the number of pores in the filter. As the number of pores increases, the pores become closer together and the stream tube/pore radius ratio approaches unity. Figure 27 and TABLE 5 show the effect of increasing the porosity towards 100% (d_p/D_{pore} equal to 0.25). The ratio R_{crit}/β is decreasing towards 0.75 as the porosity approaches 100%. The efficiency is given by equation (4-16).

$$E = 1 - \left(\frac{R_{crit}}{\beta}\right)^2 \qquad (4\text{-}16)$$

Therefore it appears that the maximum efficiency, for a given flow rate and pore diameter, would occur for the case when β approached one, and the streamlines were straight and parallel to the pore axis. This result seems to contradict intuition. Perhaps the problem is one of divorcing the two methods of increasing porosity; that is, increasing the number of pores, or increasing the pore diameter. In these cases, the efficiency for a given particle size would be expected to decrease as the pore diameter increased. However in studying the effect of possible fluctuations in filter porosity, from filter to filter, for a given average pore diameter (this was the intent of the present investigation), the filter efficiencies presented in TABLE 5 indicate that the efficiency would increase slightly with porosity. Whether or not this effect is characteristic of the actual filter, or is an artifact of the theory, is a question the present study must leave unanswered. In either case, however, the effect is relatively small and it can be expected that small variations in the filter porosity would not greatly affect the impaction efficiency as a function of particle diameter.

TABLE 5. THE IMPACTION EFFICIENCY AND THE RATIO R_{CRIT}/β AS THE POROSITY APPROACHES 100%

Porosity	R_{crit}/β	Impaction Efficiency
8%	0.8117	34.1%
10%	0.7940	36.9%
12%	0.7800	39.2%
100%	0.75	43.75%

BEGIN FIRST LINE OF TEXT HERE
TYPING GUIDE SHEET
CENTER OF PAGE
TOP OF IMAGE AREA
DROPPED HEAD; BEGIN SECTIONS HERE

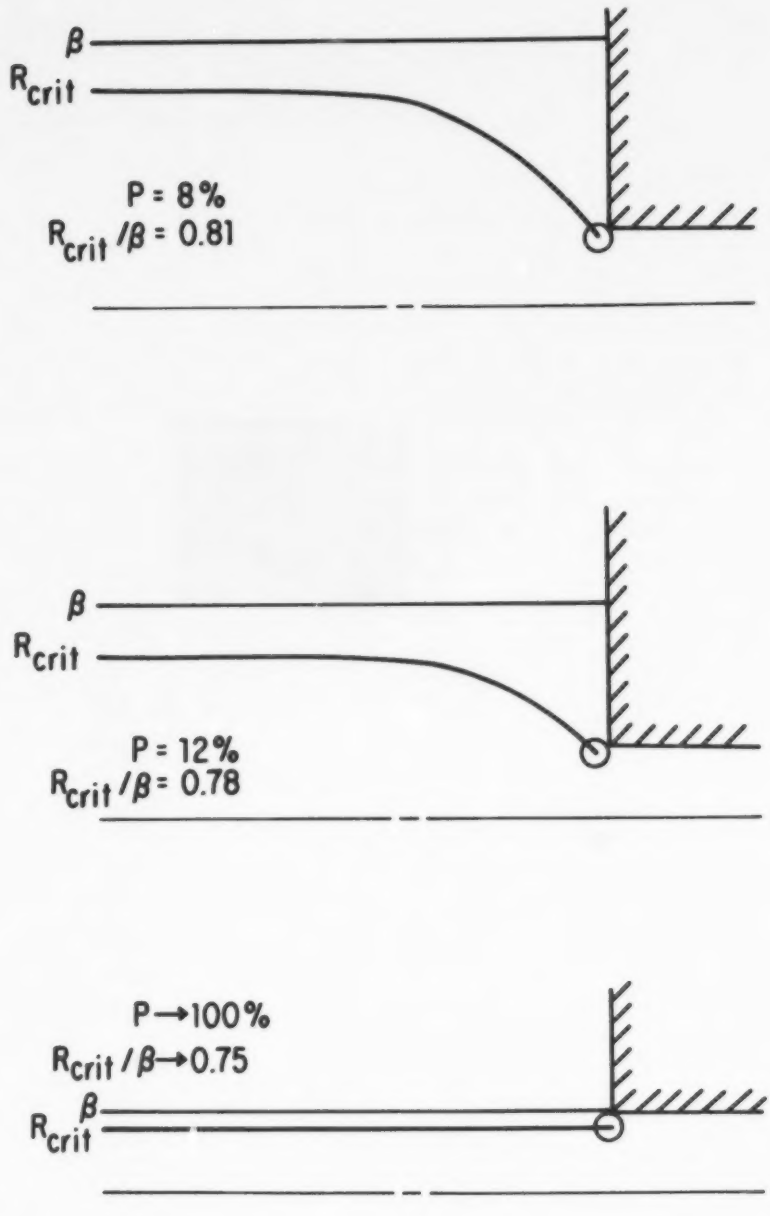

Figure 27. Illustration of the ratio of R_{crit}/β as the porosity approaches 100%.

BEGIN LAST LINE OF TEXT
BOTTOM OF IMAGE AREA; OUTSIDE DIMENSION FOR TABLES AND ILLUSTRATIONS
3/8"

EPA-287 (Cin.)
(4-76)

SECTION 6

EXPERIMENTAL COLLECTION EFFICIENCIES

INTRODUCTION

The theoretical procedures developed in the preceding sections constitute a fundamental model for the impaction efficiency. Significant assumptions have gone into the model and require experimental validation. Prominent among these assumptions were the neglection of electrostatic forces, the effect of the random distribution of pores, and the geometric model of a sudden contraction followed by a sudden expansion within a streamtube. Subject to a valid particle capture model, this impaction model is readily converted into a collection efficiency model. In the discussions that have preceded, it has been assumed that a particle that impacts the filter surface is captured by the surface. Subject to this assumption, the impaction efficiency and the collection efficiency are equal.

Collection efficiency experiments were conducted with a wet, sticky aerosol (oleic acid) with the view that such an aerosol would indeed be captured upon impact. The results of these experiments are in agreement with the theory and are accepted as validation of the impaction theory. Additional experiments were conducted with a solid aerosol (methylene blue dye) and directed at the question of particle capture. The results of these experiments gave a clear indication that the solid aerosol was not necessarily being captured upon impact, and that the particles had a tendency to bounce upon impact, become reentrained in the flow field, and pass on through the filter.

EXPERIMENTAL PROCEDURES

Using a 9.5μm pore diameter Nuclepore surface as a primary filter and a 0.4μm pore diameter Nuclepore surface as a secondary or back-up filter, collection efficiencies were measured for both liquid and solid aerosols with particle diameters ranging from 2 to 9μm. All particles not captured by the primary filter were assumed captured by the secondary filter. Collection efficiencies were determined for the primary filter. Particles were collected by a sampler employing a stacked primary and secondary filter and operating at a face velocity of 10 cm/s and 20 cm/s. Face velocity is defined as the volumetric flow rate divided by the total frontal area of the filter surface.

Both aerosols were generated using a vibrating orifice generator, as described by Berglund and Liu (21), equipped with a 20μm orifice. Several

problems were encountered in the course of generating the particles for the experiments. The generator operates on the principle of placing a known concentration of the desired aerosol material in solution in a volatile solvent, generating a known size droplet, and driving off the solvent to obtain a known size particle. Although the air supply to the generator was first passed through a very effective air dryer, we experienced considerable evidence of wet particles at the discharge from the charge neutralizer/drying tower of the generator. This was evidenced by collection efficiencies that were inordinately large (suggesting over sized particles) and by particles that were gluing themselves to the filter surface. This problem was solved by directing the discharge from the charge neutralizer vertically into a large stainless steel stilling chamber (roughly 600 l) and sampling from the lower regions of the chamber. No further evidence of wet particles was encountered. The liquid aerosol was generated using oleic acid in solution with a mixture of four parts 95 percent ethyl alcohol and one part distilled water by volume. No further difficulties were encountered in the generation of the liquid aerosol.

Generation of a satisfactory solid aerosol posed additional problems. With a liquid in solution in a solvent, driving off of the solvent is certain to produce a spherical droplet. With a solid dissolved in a solvent, driving off of the solvent is apt to result in almost any geometry or structure. It could be spherical or it could be irregular. It could be solid, hollow, or porous. While any combination of the above could describe one or more naturally occurring aerosols, the theory being tested was built around the assumption of a spherical particle of known size and mass. The difficulty encountered in trying to generate such a particle seemed to center around selecting the proper solid and solvent. The solid aerosol most commonly reported in the literature is methylene blue dye. Neither laboratory grade nor technical grade methylene blue dye (supplied by Fisher Scientific) was sufficiently soluble in aqueous ethyl alcohol to prevent clogging of the generator. The laboratory grade dye was, however, adequately soluble in methyl alcohol and was found to produce fairly spherical particles. Small amounts of distilled water were added to the solution in the hope of enhancing the spheroidicity of the particles, but the addition of water appeared to detract from the spheroidicity and to promote angularity in the particles. A solution of laboratory grade methylene blue dye dissolved in anhydrous methyl alcohol was used to generate the solid aerosol particles.

Analysis of the filter for the quantity of aerosol collected was done by means of optical fluorescence. Both solutions used in generating the aerosol particles contained a known quantity of sodium fluorescein (uranine) dye. After collecting the sample, the filters were washed in a known volume of aqueous ethyl alcohol which was subsequently analyzed with a calibrated optical fluorimeter. The aqueous ethyl alcohol, four parts 95 percent ethyl alcohol and one part distilled water by volume, was buffered five percent by volume with 1/10 normal aqueous sodium hydroxide to counter the acidity of the aerosol material and the effect of pH upon the fluorescent properties of the uranine dye. The output from the fluorimeter was sufficiently linear to permit the calculation of the collection efficiency on the basis of the instrument output for the solution from the primary filter divided by the sum of the outputs from the two solutions. The output of the fluorimeter was calibrated against known dilutions of the solution being run through the

aerosol generator and was spot checked for drift against a single dilution periodically during the data run. The calibration was used to estimate the mass loading of aerosol on the filter. In the case of oleic acid, the sensitivity of the fluorimeter was sufficient to allow the use of one part uranine dye to twenty parts oleic acid by mass. The intensity of the methylene blue dye so masked the fluorescence of the uranine dye as to require one part uranine dye to four parts methylene blue dye by mass.

The density of the oleic acid was taken to be 0.894 g/cm^3 from handbook data. The density of the uranine dye was measured as 1.91 g/cm^3, and the density of the methylene blue dye was measured as 1.36 g/cm^3 using a gas pycnometer. Based upon these data and correcting for the uranine content, the density of the liquid aerosol was estimated to be 0.92 g/cm^3 and the density of the solid aerosol was estimated to be 1.44 g/cm^3. It should be pointed out that dye composition is quite variable. The first uranine dye that we tried to use proved to be roughly 50 percent sodium chloride. Uncertainty of composition leads to uncertainties as to density and solubility.

RESULTS

The experimental results are summarized in Figures 28 and 29 along with the theory developed earlier. Shown in Figure 28 are data gathered at a face velocity of 10 cm/s. Circles indicate data for oleic acid (density = 0.92 g/cm^3) and diamonds indicate data for methylene blue dye (density = 1.44 g/cm^3). The solid curves show the collection efficiencies predicted by the theory for a range of particle densities that bracket the experimental data. Similar data are contained in Figure 29 but for a face velocity of 20 cm/s. The oleic acid data presented in both figures agree with the theoretical curves and support the model. The methylene blue dye data presented in Figure 28 fall significantly below the theoretical curves and in general below rather than above the experimental data for the less dense oleic acid particles. The methylene blue dye data presented in Figure 29 and taken at a greater face velocity than that in Figure 28 show the same general trends seen in Figure 28 but at the higher face velocity they are more dramatic. It appears reasonable to assume that the sticky oleic acid aerosol has been captured upon impact with the filter surface. On the basis of this assumption, the conclusion to be drawn from Figures 28 and 29 is that the theory developed in SECTION 3 and 4 is a valid impaction model. It appears reasonable that the theory is correctly predicting the impaction of the methylene blue dye particles upon the filter surface but that the particles are not necessarily being captured upon impact. That the deviation seen in the solid aerosol data becomes greater with increased face velocity or particle size is indicative of an inertial effect and points toward the probability of particle bounce. In the data gathered, there was no evidence that the collection efficiency was time dependent as would be the case were a particle to be captured and then dislodged upon impact from a subsequent particle. The results seen in Figures 28 and 29 show general agreement with those recently published by John et al. (22).

BEGIN FIRST LINE OF TEXT HERE
TYPING GUIDE SHEET
CENTER OF PAGE
TOP OF IMAGE AREA
DROPPED HEAD; BEGIN SECTIONS HERE

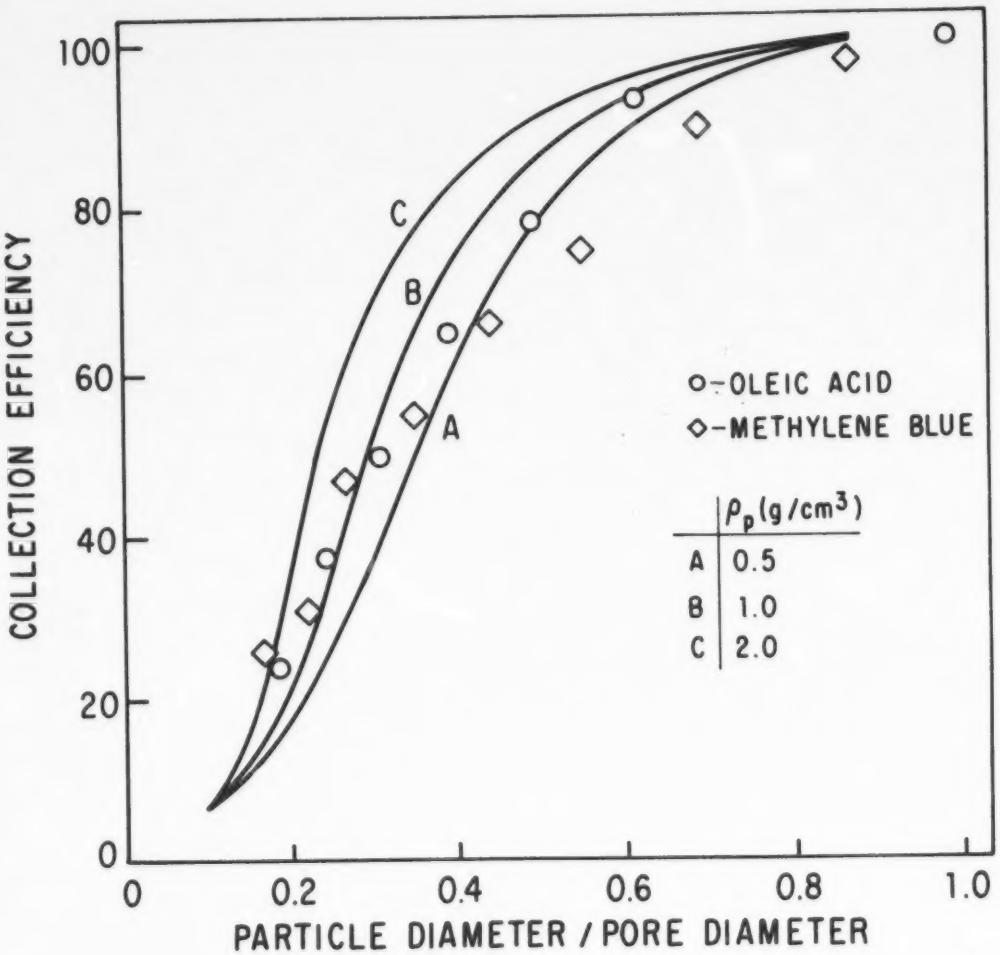

Figure 28. Experimental collection efficiencies compared with the model. Face velocity = 10 cm/s

BEGIN LAST LINE OF TEXT
BOTTOM OF IMAGE AREA; OUTSIDE DIMENSION FOR TABLES AND ILLUSTRATIONS
3/8"

EPA-287 (Cin.)
(4-76)

BEGIN FIRST LINE OF TEXT HERE
TYPING GUIDE SHEET
CENTER OF PAGE
TOP OF IMAGE AREA
DROPPED HEAD; BEGIN SECTIONS HERE

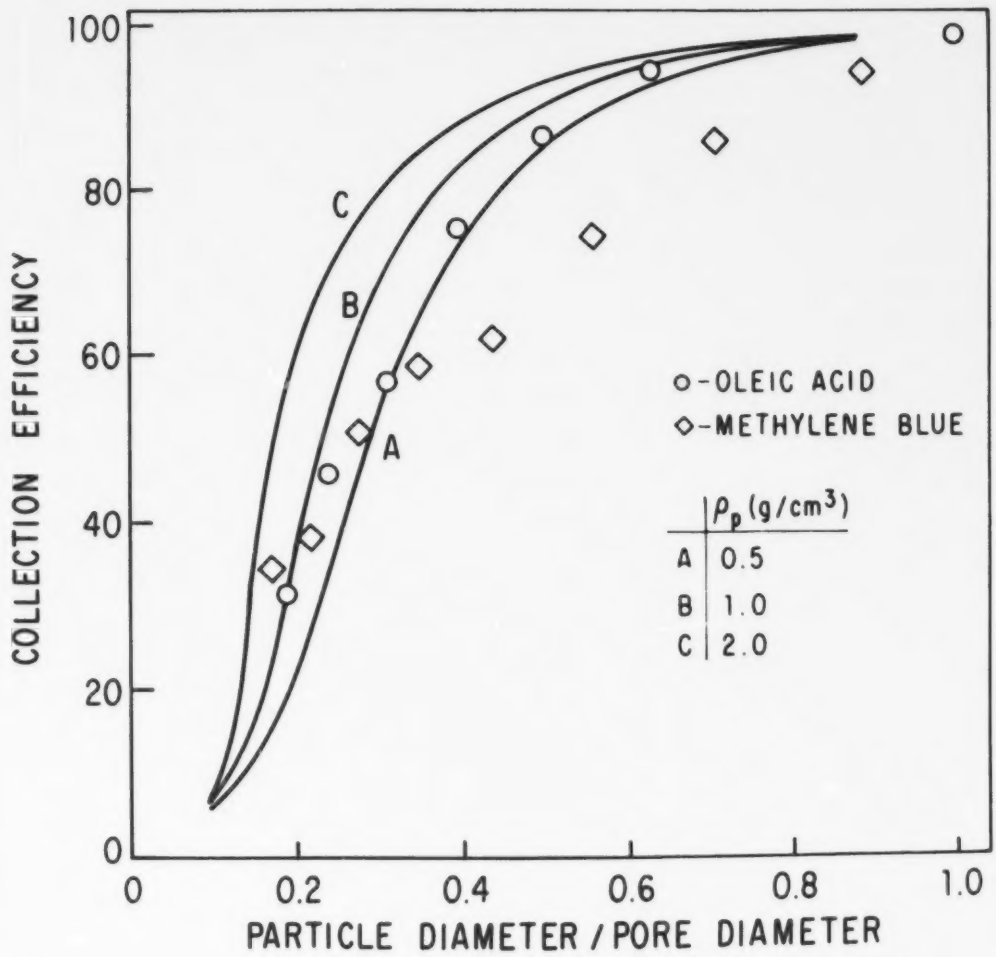

Figure 29. Experimental collection efficiencies compared with the model. Face velocity = 20 cm/s

BEGIN LAST LINE OF TEXT
BOTTOM OF IMAGE AREA OUTSIDE DIMENSION FOR TABLES AND ILLUSTRATIONS
3/8"

EPA-287 (Cin.)
(4-76)

In presenting the experimental data shown in Figures 28 and 29 it should be noted that considerable question surrounded the physical properties of the filters. The filters were Nuclepore surfaces mounted in frames and supplied by Ghia Corporation. As ordered they were to have been 12μm pore diameter with a nominal pore density of 10^5 pores/cm^2. Our initial attempts to size the pores optically at Duke University indicated a pore diameter of approximately 12μm, a pore density of approximately 0.89×10^5, and a porosity of slightly over 10 percent. For this reason most of our theoretical effort centered on a porosity of 10 percent or slight variations from it. Inspection of our initial experimental collection efficiencies indicated that either our model was in error or the filters were not what we thought them to be. A second attempt to size the pores optically at Duke University revealed that, at the magnification required to size a 12μm pore, the edge of the pore appears as a halo and could be sized anywhere from 10 to 12μm. Ultimately Ghia Corporation reported that samples from the filter stock had been sized against a certified grating under a scanning electron microscope and that the average pore diameter was 9.5μm. This reduced pore diameter leads to a filter porosity of slightly over 6 percent. The theoretical curves contained in Figures 28 and 29 were obtained assuming a filter porosity of 10 percent. This is not seen to be a serious problem. The face velocities used to obtain the experimental data are related to the pore Reynolds numbers of the theoretical curves by the correct porosity of the filter stock. The results of SECTION 5 would indicate that this variation in porosity would have little effect upon the collection efficiency. Beyond being a matter of record, this information is presented for the benefit of those familiar with Nuclepore surfaces. Our experience has been that the pore density is rather consistent at 10^5 pores/cm^2 and that a Nuclepore filter with a pore diameter of 9.5μm and a porosity of 10 percent would be unlikely.

Along with the information contained in Figures 28 and 29, a limited amount of information was gathered on the effect of filter loading. There was no evidence that filter loading was a significant factor below a loading rate of approximately 400 μg/cm^2. Above this level one could clearly observe an increased collection efficiency that was indicative of bore blockage.

REFERENCES

1. Whitby, K., R. Husar, and B. Liu. Aerosol Size Distribution of Los Angeles Smog. J. Colloid Interface Sci., 39(1):177-204, 1972.

2. Hatch, T., and P. Gross. Pulmonary Deposition and Retention of Inhaled Aerosols. Academic Press, New York, 1964.

3. Spurny, K., and J. Pich. Diffusion and Impaction Precipitation of Aerosol Particles by Membrane Ultrafilters. Collect. Czech. Chem. Commun., 30:2276-2287, 1965.

4. Pich, J. Impaction of Aerosol Particles in the Neighbourhood of a Circular Hole. Collect. Czech. Chem. Commun., 29:2223-2227, 1964.

5. Smutek, M., and J. Pich. Impaction of Particles on the Surface of Membrane Filters. Aerosol Sci., 5:17-24, 1974.

6. Smith, T., and C. Phillips. Inertial Collection of Aerosol Particles at Circular Aperture. Environ. Sci. Technol., 9(6):564-568, 1975.

7. Spurny, K., J. Lodge, Jr., E. Frank, and D. Sheesley. Aerosol Filtration by Means of Nuclepore Filters: Structural and Filtration Properties. Environ. Sci. Technol., 3(5):453-464, 1969.

8. Spurny, K., and G. Madelaine. Efficiency Measurement of Nuclear Pore Filters by Means of Latex Aerosols. Collect. Czech. Chem. Commun., 36:2857-2866, 1971.

9. Gormley, P., and M. Kennedy. Proc. Roy. Irish Acad., 52A:163-169, 1949.

10. Stern, S., H. Zeller, and A. Schekman. Collection Efficiency of Jet Impactors at Reduced Pressures. I. and E.C. Fundamentals, 1(4):273-277, 1962.

11. Millikan, R. Phys. Rev., 22(1), 1923.

12. Cahill, T., R. Eldred, J. Barone, and L. Ashbaugh. Ambient Aerosol Sampling with Stacked Filter Units. FHWA-RD-78-178, Federal Highway Administration, Washington, D.C., 1979.

13. Vrentas, J., J. Duda, and K. Bargeron. Effect of Axial Diffusion of Vorticity on Flow Development in Circular Conduits: Numerical Solutions. A. I. Ch. E. J., 12(5), 1966.

14. Vrentas, J., and J. Duda. Flow of a Newtonian Fluid Through a Sudden Contraction. App. Sci. Res., 38:241-260, 1973.

15. Schlichting, H. Boundary Layer Theory. McGraw-Hill, New York, 1968.

16. Forsythe, G., and W. Wason. Finite-Difference Methods for Partial Differential Equations. John Wiley and Sons, New York, 1960.

17. Parker, R.D. A Fundamental Study of Particle Deposition onto Large Pore Nuclepore Filters. Ph.D. Thesis, Duke University, Durham, North Carolina, 1975. (Available through University Microfilms).

18. Marple, V., and B. Liu. Characteristics of Laminar Jet Impactors. Environ. Sci, Technol., 8(7):648-654, 1974.

19. Carnahan, B., H. Luther, and J. Wilkes. Applied Numerical Methods. John Wiley and Sons, New York, 1969.

20. Collatz, L. The Numerical Treatment of Differential Equations. Springer-Verlag, Berlin, 1960.

21. Berglund, R. N., and B. Y. H. Liu. Generation of Monodisperse Aerosol Standards. Environ. Sci. Technol., 7:147-153, 1973.

22. John, W., G. Reischl, S. Goren, and D. Plotkin. Anomalous Filtration of Solid Particles by Nuclepore Filters. Atmos. Environ., 12:1555-1557, 1978.

APPENDIX A

FINITE DIFFERENCE EQUATIONS

CENTRAL DIFFERENCE DERIVATIVE APPROXIMATIONS

Central difference approximations to first and second derivatives may be obtained from Taylor series expansions in the standard manner. For an arbitrary function F, in an arbitrary direction x, with a uniform grid spacing h, the approximations are[1]

$$\frac{\partial F}{\partial x} = \frac{1}{2h}\left(F_{x+h} - F_{x-h}\right) \tag{A-1}$$

$$\frac{\partial^2 F}{\partial x^2} = \frac{1}{h^2}\left(F_{x+h} - 2F_x + F_{x-h}\right) \tag{A-2}$$

For a nonuniform grid spacing h_e and h_w,

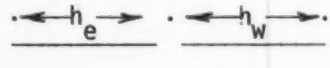

the approximations are[1]

$$\frac{\partial F}{\partial x} = \left(\frac{h_w}{h_e(h_e+h_w)}\right)F_{x+h_e} + \left(\frac{h_e - h_w}{h_e h_w}\right)F_x - \left(\frac{h_e}{h_w(h_e+h_w)}\right)F_{x-h_w} \tag{A-3}$$

$$\frac{\partial^2 F}{\partial x^2} = \left(\frac{2}{h_e(h_e + h_w)}\right)F_{x+h_e} - \left(\frac{2}{h_e h_w}\right)F_x + \left(\frac{2}{h_w(h_e + h_w)}\right)F_{x-h_w} \tag{A-4}$$

---

[1]These equations are derived in detail by Forsythe and Wasow (16), pp. 184-195.

COEFFICIENTS FOR THE DIFFERENCE FORMS OF THE GOVERNING EQUATIONS

The finite difference forms of the governing equations were presented in SECTION 3 as equations (3-24) and (3-25).

$$\omega_{i,j} = C_o(C_1\omega_{i,j+1} + C_2\omega_{i,j-1} + C_3\omega_{i+1,j} + C_4\omega_{i-1,j}) \tag{3-24}$$

$$\psi_{i,j} = D_o(D_1\psi_{i,j+1} + D_2\psi_{i,j-1} + D_3\psi_{i+1,j} + D_4\psi_{i-1,j} - \omega_{i,j}) \tag{3-25}$$

These equations were obtained by substituting equations (A-1), (A-2), (A-3), and (A-4) into equations (3-16) and (3-17), or into equations (3-20) and (3-21). For the upstream and downstream regions, equations (3-20) and (3-21) were the governing equations. In the pore region, equations (3-16) and (3-17) were used. The variable grid size derivative approximations, equations (A-3) and (A-4), were needed for the pore entrance and exit planes, and for the last but one radial grid line in the upstream and downstream regions. The coefficients for equations (3-24) and (3-25) are presented below for the various regions. In all cases, it should be understood that Re, X_1, and X_2 are given by equations (3-12), (3-22), and (3-23) respectively. Also the symbols h, k, and η are understood to be h_u, k_u, and η_u upstream, and to be h_d, k_d, η_d downstream of the filter.

Upstream and Downstream Coefficients

The following coefficients are valid upstream and downstream, except on the last but one radial grid line.

$$C_o = \left(\frac{2X_1^2}{h^2} + \frac{2}{h_R^2} + \frac{1}{R^2} - \frac{ReX_1}{4R^2h}(\psi_{i,j+1} - \psi_{i,j-1})\right)^{-1} \tag{A-5}$$

$$C_1 = \frac{X_1^2}{h^2} + \frac{X_2}{2h} + \frac{Re\ X_1}{8Rh_Rh}(\psi_{i+1,j} - \psi_{i-1,j}) \tag{A-6}$$

$$C_2 = \frac{X_1^2}{h^2} - \frac{X_2}{2h} - \frac{Re\ X_1}{8Rh_Rh}(\psi_{i+1,j} - \psi_{i-1,j}) \tag{A-7}$$

$$C_3 = \frac{1}{h_R^2} + \frac{1}{2Rh_R} - \frac{Re\ X_1}{8Rh_Rh}(\psi_{i,j+1} - \psi_{i,j-1}) \tag{A-8}$$

$$C_4 = \frac{1}{h_R^2} - \frac{1}{2Rh_R} + \frac{Re\ X_1}{8Rh_R h}\left(\psi_{i,j+1} - \psi_{i,j-1}\right) \qquad \text{(A-9)}$$

$$D_o = \left(\frac{2X_1^2}{Rh^2} + \frac{2}{Rh_R^2}\right)^{-1} \qquad \text{(A-10)}$$

$$D_1 = \frac{X_1^2}{Rh^2} + \frac{X_2}{2Rh} \qquad \text{(A-11)}$$

$$D_2 = \frac{X_1^2}{Rh^2} - \frac{X_2}{2Rh} \qquad \text{(A-12)}$$

$$D_3 = \frac{1}{Rh_R^2} - \frac{1}{2R^2 h_R} \qquad \text{(A-13)}$$

$$D_4 = \frac{1}{Rh_R^2} + \frac{1}{2R^2 h_R} \qquad \text{(A-14)}$$

Coefficients for the Last But One Radial Grid Line

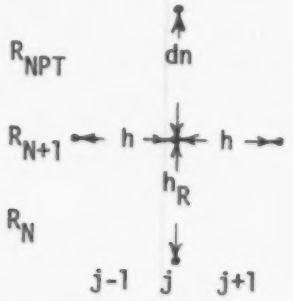

$$C_o = \left(\frac{ReX_1}{4Rh}\left(\psi_{N+1,J+1} - \psi_{N+1,J-1}\right)\left(A_2 - \frac{1}{R}\right) + \frac{2X_1^2}{h^2} - B_2 - \frac{A_2}{R} + \frac{1}{R^2}\right)^{-1} \qquad \text{(A-15)}$$

$$C_1 = \frac{X_1^2}{h^2} + \frac{X_2}{2h} + \frac{ReX_1}{4Rh}\left(A_1\psi_{NPT,j} + A_2\psi_{N+1,j} + A_3\psi_{N,j}\right) \quad \text{(A-16)}$$

$$C_2 = \frac{X_1^2}{h^2} - \frac{X_2}{2h} - \frac{ReX_1}{4Rh}\left(A_1\psi_{NPT,j} + A_2\psi_{N+1,j} + A_3\psi_{N,j}\right) \quad \text{(A-17)}$$

$$C_3 = B_1 + \frac{A_1}{R} - A_1\frac{ReX_1}{4Rh}\left(\psi_{N+1,j+1} - \psi_{N+1,j-1}\right) \quad \text{(A-18)}$$

$$C_4 = B_3 + \frac{A_3}{R} - A_3\frac{ReX_1}{4Rh}\left(\psi_{N+1,j+1} - \psi_{N+1,j-1}\right) \quad \text{(A-19)}$$

$$D_o = \left(\frac{2X_1^2}{Rh^2} - \frac{B_2}{R} + \frac{A_2}{R^2}\right)^{-1} \quad \text{(A-20)}$$

$$D_1 = \frac{X_1^2}{Rh^2} + \frac{X_2}{2Rh} \quad \text{(A-21)}$$

$$D_2 = \frac{X_1^2}{Rh^2} - \frac{X_2}{2Rh} \quad \text{(A-22)}$$

$$D_3 = \frac{B_1}{R} - \frac{A_1}{R^2} \quad \text{(A-23)}$$

$$D_4 = \frac{B_3}{R} - \frac{A_3}{R^2} \quad \text{(A-24)}$$

where the A_i abd B_i are the variable grid size coefficients, given by

$$A_1 = \frac{h_R}{dn(h_R + dn)} \quad \text{(A-25)}$$

$$A_2 = \frac{dn - h_R}{dn\ h_R} \tag{A-26}$$

$$A_3 = \frac{-dn}{h_R(h_R + dn)} \tag{A-27}$$

$$B_1 = \frac{2}{dn(h_R + dn)} \tag{A-28}$$

$$B_2 = \frac{-2}{dn\ h_R} \tag{A-29}$$

$$B_3 = \frac{2}{h_R(h_R + dn)} \tag{A-30}$$

Coefficients in the Pore Region

The following coefficients are valid in the pore entrance and exit planes as well as inside the pores.

$$C_o = \left(\frac{2}{h_R^2} + \frac{1}{R^2} + \frac{2}{h_e h_w} - \frac{Re\ B}{4Rh_R}\left(\frac{h_w}{h_e(h_e + h_w)}\right) - \frac{ReA}{2R^2}\right)^{-1} \tag{A-31}$$

$$C_1 = \frac{2}{he(h_e + h_w)} + \frac{Re\ B}{4Rh_R}\left(\frac{h_w}{h_e(h_e + h_w)}\right) \tag{A-32}$$

$$C_2 = \frac{2}{h_w(h_e + h_w)} - \frac{Re\ B}{4Rh_R}\left(\frac{h_e}{h_w(h_e + h_w)}\right) \tag{A-33}$$

$$C_3 = \frac{1}{h_R^2} + \frac{1}{2Rh_R} - \frac{Re\ A}{4Rh_R} \tag{A-34}$$

$$C_4 = \frac{1}{h_R^2} - \frac{1}{4Rh_R} + \frac{Re\ A}{4Rh_R} \qquad \text{(A-35)}$$

$$D_o = \left(\frac{2}{Rh_R^2} + \frac{2}{Rh_e h_w}\right)^{-1} \qquad \text{(A-36)}$$

$$D_1 = \frac{2}{Rh_e(h_e + h_w)} \qquad \text{(A-37)}$$

$$D_2 = \frac{-2}{Rh_w(h_e + h_w)} \qquad \text{(A-38)}$$

$$D_3 = \frac{1}{Rh_R^2} - \frac{1}{2R^2 h_R} \qquad \text{(A-39)}$$

$$D_4 = \frac{1}{Rh_R^2} + \frac{1}{2R^2 h_R} \qquad \text{(A-40)}$$

where

$$A = \left(\frac{h_w}{h_e(h_e + h_w)}\right)\psi_{i,j+1} + \left(\frac{h_e - h_w}{h_e\ h_w}\right)\psi_{i,j} - \left(\frac{h_e}{h_w(h_e + h_w)}\right)\psi_{i,j-1} \qquad \text{(A-41)}$$

$$B = \psi_{i+1,j} - \psi_{i-1,j} \qquad \text{(A-42)}$$

In equations (A-31) through (A-41), the proper grid spacing must be used in place of h_e and h_w. Within the pore, the grid spacing is uniform and $h_e = h_w = h_z$. At the pore entrance, $h_e = h_z$, and $h_e = (1/k_d)\tanh^{-1}(h_d)$.

APPROXIMATION FOR THE SECOND DERIVATIVE OF THE STREAM FUNCTION AT THE FILTER SURFACE

Special equations are needed to approximate the boundary condition for the vorticity on the filter surface. In SECTION 3 equation (3-26) was presented for this approximation. It requires an expression for the second derivative of the stream function in the direction normal to the surface. This expression is derived below.

Expanding ψ into two Taylor series, in the normal direction n, for uniform grid spacing, h, gives

$$\psi_{n-h} = (\psi)_{n=0} - h\left(\frac{\partial\psi}{\partial n}\right)_{n=0} + \frac{h^2}{2}\left(\frac{\partial^2\psi}{\partial n^2}\right)_{n=0} - \frac{h^3}{6}\left(\frac{\partial^3\psi}{\partial n^3}\right)_{n=0} + \ldots \qquad \text{(A-43)}$$

$$\psi_{n-2h} = (\psi)_{n=0} - 2h\left(\frac{\partial\psi}{\partial n}\right)_{n=0} + 2h^2\left(\frac{\partial^2\psi}{\partial n^2}\right)_{n=0} - \frac{4h^3}{3}\left(\frac{\partial^3\psi}{\partial n^3}\right)_{n=0} + \ldots \qquad \text{(A-44)}$$

Making use of the information,

$$(\psi)_{n=0} = \left(\frac{\partial\psi}{\partial n}\right)_{n=0} = 0$$

and eliminating $\left(\frac{\partial^3\psi}{\partial n^3}\right)_{n=0}$, from equations (A-43) and (A-44), gives

$$\left(\frac{\partial^2\psi}{\partial n^2}\right)_{n=0} = \frac{4\psi_{n-h}}{h^2} - \frac{\psi_{n-2h}}{2h^2} \qquad \text{(A-45)}$$

Equation (A-45) was used to obtain equation (3-26).

FINITE DIFFERENCE EXPRESSIONS FOR THE AXIAL VELOCITIES ON THE PORE CENTERLINE AND HYPOTHETICAL STREAM TUBE WALL

Expressions for the axial velocity on the pore centerline and on the hypothetical tube wall were obtained using the boundary conditions on U, as presented in Figure 3. That is, $\frac{\partial U}{\partial R} = 0$.

Pore Centerline

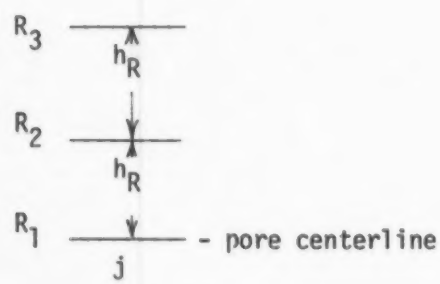

Expanding U into Taylor series from the pore centerline, R_1, gives

$$U_2 = U_1 + h_R \left(\frac{\partial U}{\partial R}\right)_1 + \frac{h_R^2}{2}\left(\frac{\partial^2 U}{\partial R^2}\right)_1 + \ldots \qquad \text{(A-46)}$$

$$U_3 = U_1 + 2h_R\left(\frac{\partial U}{\partial R}\right)_1 + 2h_R^2\left(\frac{\partial^2 U}{\partial R^2}\right) + \ldots \qquad \text{(A-47)}$$

Multiplying equation (A-46) by 4 and subtracting from it equation (A-47) gives

$$4U_2 - U_3 = 3U_1 + 2h_R \left(\frac{\partial U}{\partial R}\right)_1$$

Noting that $\left(\frac{U}{R}\right)_1 = 0$, and solving for U_1 gives

$$U_1 = \frac{4U_2 - U_3}{3} \qquad \text{(A-48)}$$

Equation (A-48) is equivalent to equation (4-1).

Hypothetical Stream Tube Wall

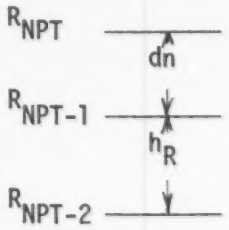

Expanding U into two Taylor series, from R_{NPT} gives

$$U_{NPT-1} = U_{NPT} - dn\left(\frac{\partial U}{\partial R}\right)_{NPT} + \frac{dn^2}{2}\left(\frac{\partial^2 U}{\partial R^2}\right)_{NPT} - \ldots \qquad \text{(A-49)}$$

$$U_{NPT-2} = U_{NPT} - (h_R + dn)\left(\frac{\partial U}{\partial R}\right)_{NPT} + \frac{(h_R+dn)^2}{2}\left(\frac{\partial^2 U}{\partial R^2}\right)_{NPT} - \ldots \qquad \text{(A-50)}$$

Multiplying equation (A-49) by $\left(\frac{h_R + dn}{h_R\ dn}\right)$, multiplying equation (A-50) by $\left(\frac{dn}{h_R(h_R + dn)}\right)$, and subtracting the resultant equations yields

$$\left(\frac{h_R + dn}{h_R\ dn}\right) U_{NPT-1} - \left(\frac{dn}{h_R(h_R + dn)}\right) U_{NPT-2} = \left(\frac{h_R + dn}{h_R\ dn} - \frac{dn}{h_R(h_R + dn)}\right) U_{NPT}$$

$$- \left(\frac{h_R + dn}{h_R} - \frac{dn}{h_R}\right) \left(\frac{\partial U}{\partial R}\right)_{NPT}$$

Noting that $\left(\frac{\partial U}{\partial R}\right)_{NPT} = 0$, gives

$$U_{NPT} = \frac{\left(\frac{h_R+dn}{h_R\ dn}\right) U_{NPT-1} - \left(\frac{dn}{h_R(h_R+dn)}\right) U_{NPT-2}}{\left(\frac{h_R+dn}{h_R\ dn} - \frac{dn}{h_R(h_R+dn)}\right)} \qquad \text{(A-51)}$$

Equation (A-51) is equivalent to equation (4-2).